Interreg
Italia-Österreich
European Regional Development Fund
EUROPEAN UNION
AUTONOME PROVINZ BOZEN SÜDTIROL
PROVINCIA AUTONOMA DI BOLZANO ALTO ADIGE
ALMA MATER STUDIORUM UNIVERSITÀ DI BOLOGNA

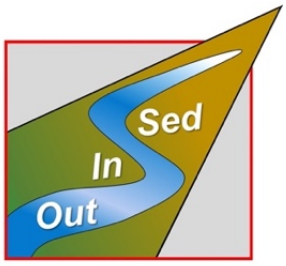

SedInOut

Development of a risk management methodology through the assessment of sediment availability for mass wasting activity in mountain environments

Sediment characterisation and analysis (WP 5 & WP 6)

Volkmar Mair[1], Monika Rabanser[1], Riccardo Scotti[2] Francesco Brardinoni[3]

[1]Amt für Geologie und Baustoffprüfung, Autonome Provinz Bozen
[2] Servizio Glaciologico Lombardo (SGL)
[3]Dipartimento di Scienze Biologiche, Geologiche e Ambientali, Università Bologna (BiGea)

Table of contents

1. Introduction and report structure

Contemporary atmospheric temperature rise imposes profound physical changes to high-elevation mountain environments. These changes, by directly affecting the mountain cryosphere through glacier retreat and permafrost degradation, can alter the hydrologic regime of mountain drainage basins (Huggel et al., 2015), as well as the amount and caliber of sediment readily available for mass movements and fluvial transport. Although sediment supply exerts a primary control on channel stability and relevant geo-hazard potential, there is a general lack of standard procedures for characterizing sediment sources, sediment typology and for evaluating sediment availability. This gap, which is mainly associated with the variety of existing national and regional protocols of data collection, currently prevents pursuing an unbiased, transnational risk management strategy considering current climatic challenges. SedInOut, through a joint international effort, aims to develop methodologies for the quantification and characterization of sediment across representative pilot catchments, towards a sustainable land management that values geo-risk mitigation and sediment recycling.

In this report, we present a methodological approach that relies on existing geological mapping (CARG project), high-resolution digital topography, and historical aerial photos and orthophoto mosaics, while integrating field-based and proximal sensing data in conjunction with multi-temporal, remotely based mapping (**Figure 1).** Remotely sensed procedures include multi-temporal mapping of glacier extent (**Section 3.1.1**), Quaternary materials (e.g., bedrock, glacial till, talus debris, colluvium, and alluvium) (**Section 3.1.2**), the drainage network (**Section 3.1.3**) and rapid shallow failures (i.e., sediment sources including debris slides, debris flows and bank collapses) (**Section 3.1.4**). Field-based and proximal sensing data include measurements on shallow landslide geometry (**Section 3.2.1**), and characterization of surface (i.e., manual Wolman pebble count and photo sieving) and subsurface (i.e., bulk sampling, on-site preliminary sieving, and laboratory sieving) grain size distribution (GSD) conducted at six representative sites (i.e., M1 through M6; **Figure 2a**) along the mountain channel network that drains the glaciated landscape of Upper Mazia Valley (**Sections 3.2.2**, **3.2.3**, **3.3**, and **3.4**). Field measurements on landslide geometry are critical for constraining an empirical landslide area-volume relation, which in turn is used for translating landslide areas, as mapped on sequential photo sets, into first-order volumetric estimates of mobilized debris. GSD data allows characterizing the spatial variability of characteristic sediment calibers (i.e., D_{50}, D_{84}, and D_{90}) as well as the armoring ratio (an index of channel stability), starting at glacier and rock glacier fronts and moving downstream.

The multi-temporal mapping approach is structured as follows. Through visual inspection of sequential orthophoto sets, we first track changes in glacier extent. Subsequently, as glaciers retreat, we map and quantify the extent of newly exposed Quaternary materials, the occurrence of shallow rapid failures, and the relevant changes in the structure of the main drainage network.

In this document, we illustrate SedInOut methodological approach applied to Mazia Valley, here regarded as representative of conditions that characterize the Austroalpine geologic domain. In particular, we integrate two nested spatial scales: (i) ***Upper Mazia Valley*** (18.8 km^2) over which we conducted extensive fieldwork to constrain the geometry of rapid shallow failures on the hillslopes and low-order streams, and to characterize alluvial sediment along the channel network **(Figure 2a**); (ii) ***Proglacial Mazia Area*** (8.4 km^2), where we document decadal geomorphological changes following the retreat of the Mazia glacier (**Figure 2b**). Time and temporal scales of investigation are summarized in **Table 1**.

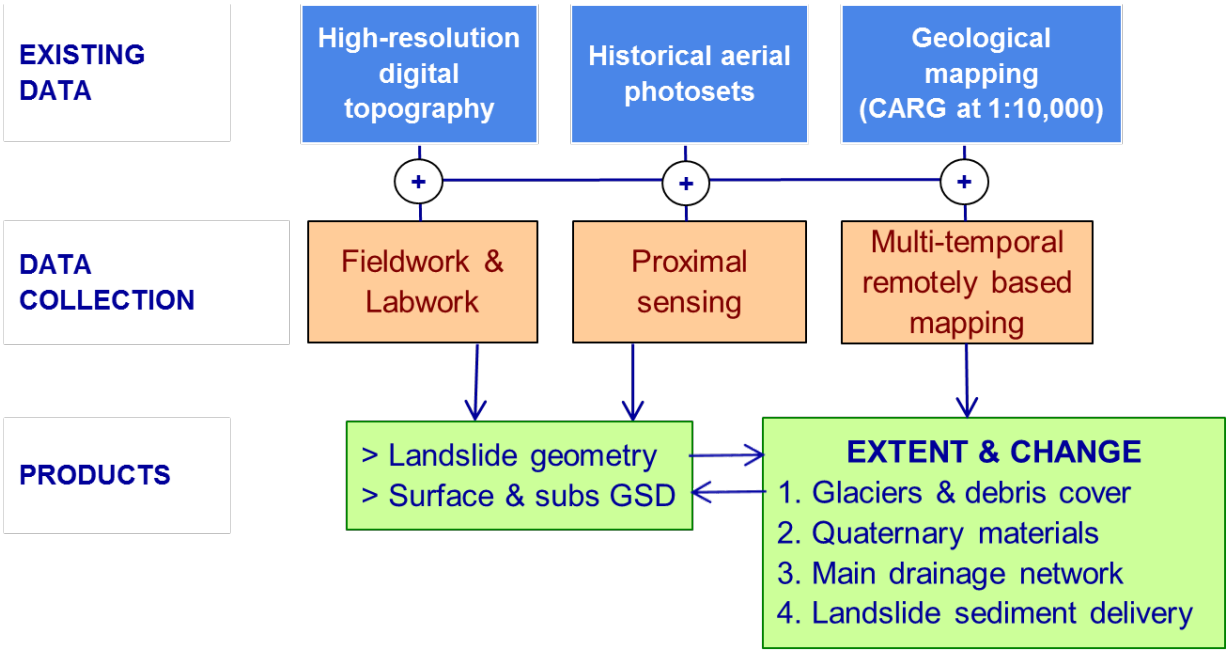

Figure 1. Scheme of the methodological approach adopted in this study.

Multi-temporal mapping	Spatial scale	Time steps
Glaciers	Upper Mazia Valley	1860-1945-69-85-94-2003-06-08-14/15-17-2020
Quaternary materials	Proglacial Mazia Area	1969-94-2006-14-16-2020
Drainage network	Proglacial Mazia Area	1969-94-2006-14-16-2020
Rapid shallow failures	Mid & Upper Mazia Valley	1959-69-82/85-97/99-2006/08-11-15-2020

Table 1. Spatial and time scales of historical, remotely based investigation in Mazia Valley.

2. Study area

The pilot study area is the upper portion of the broader Mazia Valley (90 km^2), a mountain basin drained by Saldur Creek that flows into the Adige/Etsch River in proximity of Sluderno/Schluderns, northwestern South Tyrol (**Figure 2a**). Elevation ranges from 3738 m asl (Palla Bianca/Weißkugel) down to 930 m asl at the valley outlet. The area is among the driest within the Alps (Frei and Schär, 1998), with mean annual precipitation in Silandro/Schlanders (698m a.s.l.) of 502 mm (1921–2018) (Meteo Alto Adige, 2020).

Bedrock lithology consists of polymetamorphic rocks of the Austroalpine Domain (Ötztal nappe and Matsch unit, **Figure 3**). In particular, the mid and upper Mazia Valley belongs to the Ötztal nappe (Ratschbacher et al., 1989; Thöni, 1999), that consists mainly of paragneiss and micasschists. The landscape exhibits a strong glacial imprint with the main Mazia glacial trough drained by Saldur Creek, which receives sediment inputs from lateral debris cones and fans at steep tributary confluences. Typically, tributaries originate from glaciers and rock glaciers at hanging glacial cirques, and flow down steep, rocky valley steps that in places have formed steep gorges (e.g., Oberettes Creek). The glacial and periglacial imprint is further operated by widespread occurrence of rock glaciers, and moraine ridges.

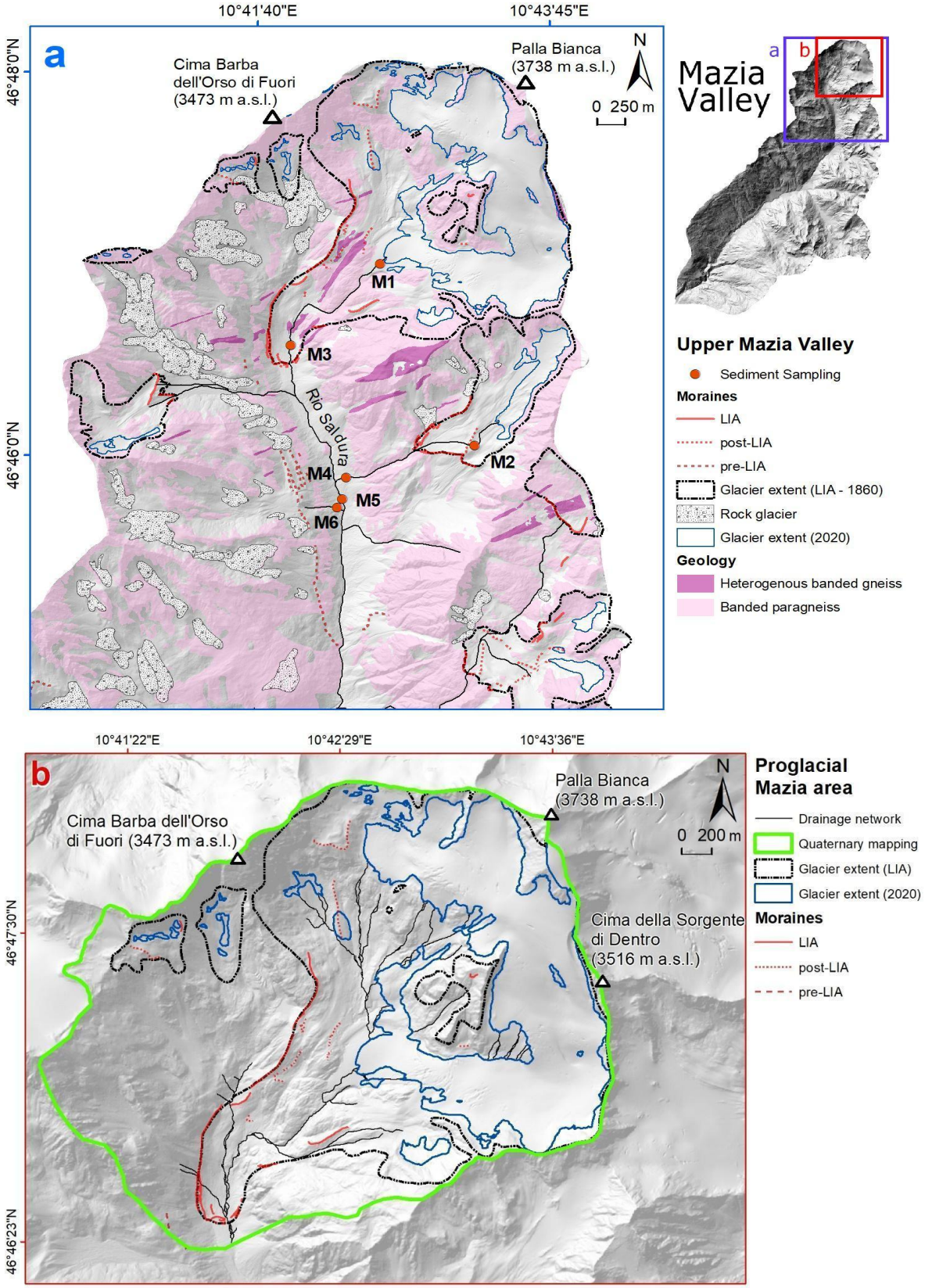

Figure 2. Maps illustrating the glacier extent during the Little Ice Age (LIA) maximum and in 2020, the spatial distribution of the relevant moraines and the location of the sediment sampling points in: (a) Upper Mazia Valley; and (b) Proglacial Mazia Area. Inset map shows the location of the two scales of investigation within the entire Mazia valley (i.e., Saldur Creek basin).

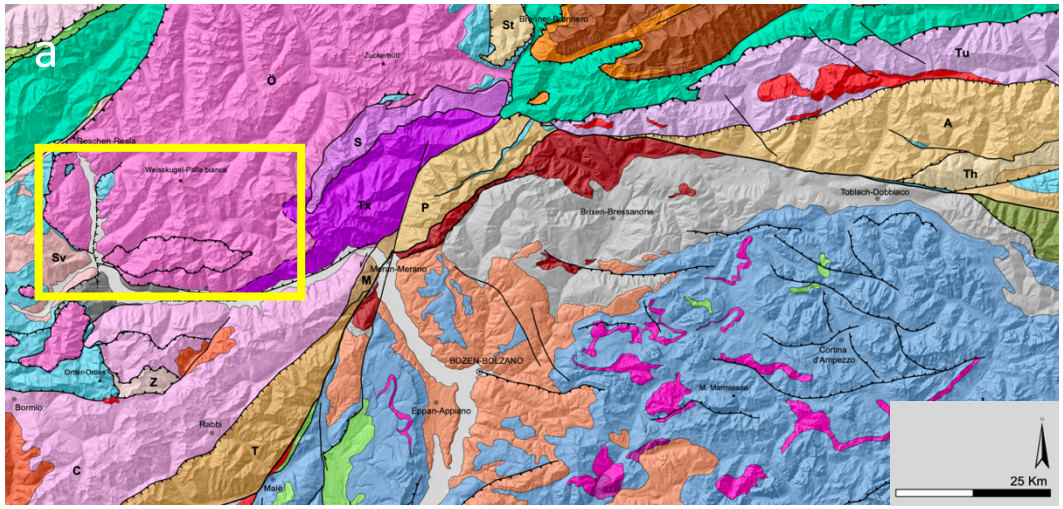

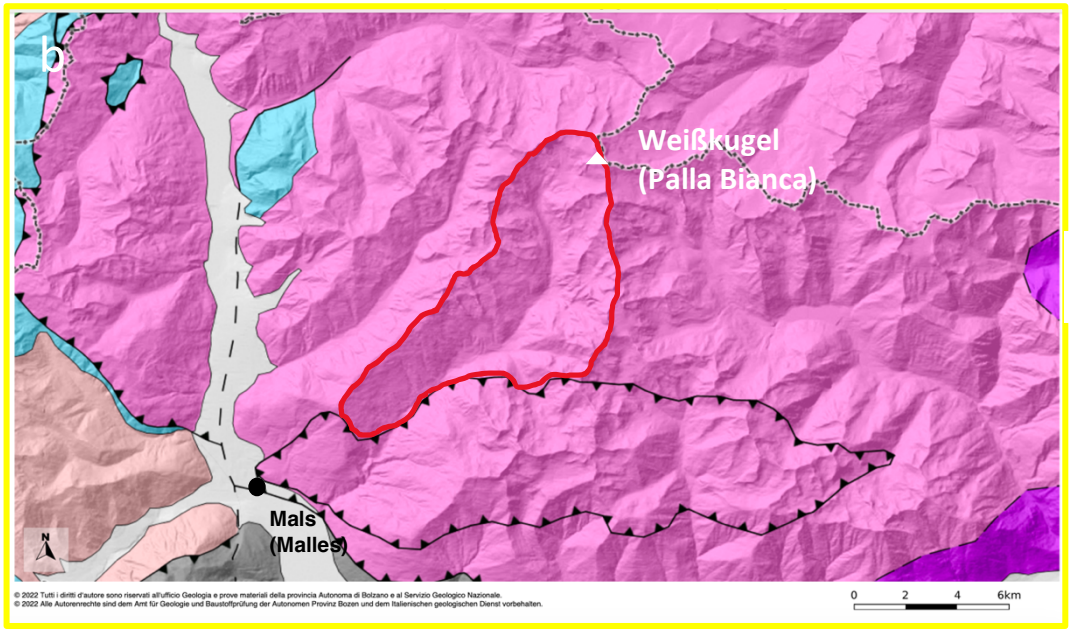

Quaternary continental deposits
Alpine Molasse
Tertiary plutons

PENNINIC UNITS

Helvetic units
Arosa-Zone (Flysch Cretaceus-Eocene)
Tasna nappe (Trias-Eocene with basement)
Calcschists with ophiolitic bodies
Old European basement nappes
Central Gneiss

SOUTHERN ALPS

Cretaceous-paleogene sediments
Permo-jurassic sediments
Triassic vulcanites and volcanoclastites
Triassic plutons
Permian vulcanites
Permian plutons
Paleozoic succesion (Alpi Carniche)
Low grade metamorphic Variscan basement
Medium grade metamorphic Variscan basement

AUSTROALPINE UNITS

Permo-mesozoic succession of the Northern Calcareous Alps
Northern paleozoic succession (Grauwackenzone)
Permo-mesozoic succession of different tectonic units
Permian plutons

CRYSTALLINE BASEMENT

Steinach nappe (St) (Low variscan and alpine metamorphic grade)
Thurntaler unit (Th) (Medium variscan and negligible alpine metamorphic grade)
Antholz unit (A) (Medium-high variscan and negligible alpine metamorphic grade)
Tectonic units of Passaier (P) (Medium-high variscan and negligible alpine metamorphic grade)
Marlinger unit (M) (Medium-high variscan and low alpine metamorphic grade)
Tonale nappe (T) (High variscan and negligible alpine metamorphic grade)
Taufers unit (Tu) (Medium-high variscan and alpine metamorphic grade)
Zebrù unit (Z) (Low variscan and negligible alpine metamorphic grade)
Ortles-Campo nappe (C) (Medium-high variscan and low alpine metamorphic grade)
Vinschgau shear zone
Sesvenna unit (Sv) (Medium-high variscan and negligible alpine metamorphic grade)
Silvretta nappe (Si) (Medium-high variscan and medium alpine metamorphic grade)
Innsbruck (I) and Landeck (L) phyllite (Low variscan and negligible alpine metamorphic grade)
Bernina nappe (B) (Medium-high variscan and low alpine metamorphic grade)

Periadriatic Line
Tectonic lines
Thrusts of mayor units
Minor thrusts
Thrusts with reactivation as normal fault
Normal faults
Strike-slip faults

Figure 3. Geological overview of the area of interest. (a) General geologic map of South Tyrol. (b) Detailed overview of the Upper Venosta Valley. The Upper Mazia valley is marked in red. Note the geological distinction between the Upper Mazia Valley (Ötztal-Stubai unit) and the lower Mazia valley (Mazia nappe). Modified after Keim, Mair and Morelli (2017).

3. Data collection and methods

3.1 Historical multi-temporal mapping

3.1.1 Glaciers

To reconstruct and quantify post-LIA (Little Ice Age) glacier area change through time, we have manually mapped the outlines of glaciers, glacierets and perennial snowfields (here all termed "glaciers") across 11 sequential time steps (**Table 1**). Mapping since 1945 has been conducted on aerial photo pairs and on orthophoto mosaics. The reconstruction of the LIA maximum glacier extent follows the procedure outlined by Scotti et al. (2014) and as such it was conducted through integration of: (i) field mapping of trimlines and the (usually) well preserved moraines; (ii) remotely-based interpretation of aerial photographs and shaded-relief rasters derived from the 2006 LiDAR-DSM (Digital Surface Model); and (iii) information on glacier extent drawn from historical maps, paintings, terrestrial photographs, technical reports and scientific literature (e.g., Knoll et al., 2009). This mapping procedure involves some degree of interpolation along glacier margins that lack reliable morphological constraints. With respect to the exact timing of the LIA maximum, in areas of the European Alps where this benchmark is not well constrained by either historical information or by dating of the relevant moraines, it is customarily referred to the advance occurred around 1860 (Holzhauser et al., 2005, Nicolussi et al., 2022).

To provide a qualitative assessment of the coarse debris load carried by the study glaciers through time and made available during deglaciation, following a classification scheme proposed by Gardent (2014), we have further mapped and classified glacier polygons into three categories according to debris cover through visual inspection of the sequential aerial photo sets (e.g., **Figure 4**). Categories include: (i) clean ice; (ii) partly debris-covered ice; and (iii) debris-covered ice (**Table 2**). Since evaluation of debris cover requires snow-free conditions, this classification is usually limited to the lower (ablating) half of the glacier, the glacier portion that essentially supplies all glaciogenic sediment directly to the proglacial area.

Category	Approximate percent cover	Description
Clean Ice	DC < 20	Clean ice mostly visible with limited patches of debris.
Partly debris-covered ice	20 ≤ DC ≤ 90	Sparse debris cover with glacier ice partly visible, and/or fine sediment cover and ice surface morphology still visible.
Debris-covered ice	DC ≥ 90	Complete debris cover, except from small ice windows associated with crevasses.

Table 2. Classification of glacier ice surface with respect to debris cover (DC) extent.

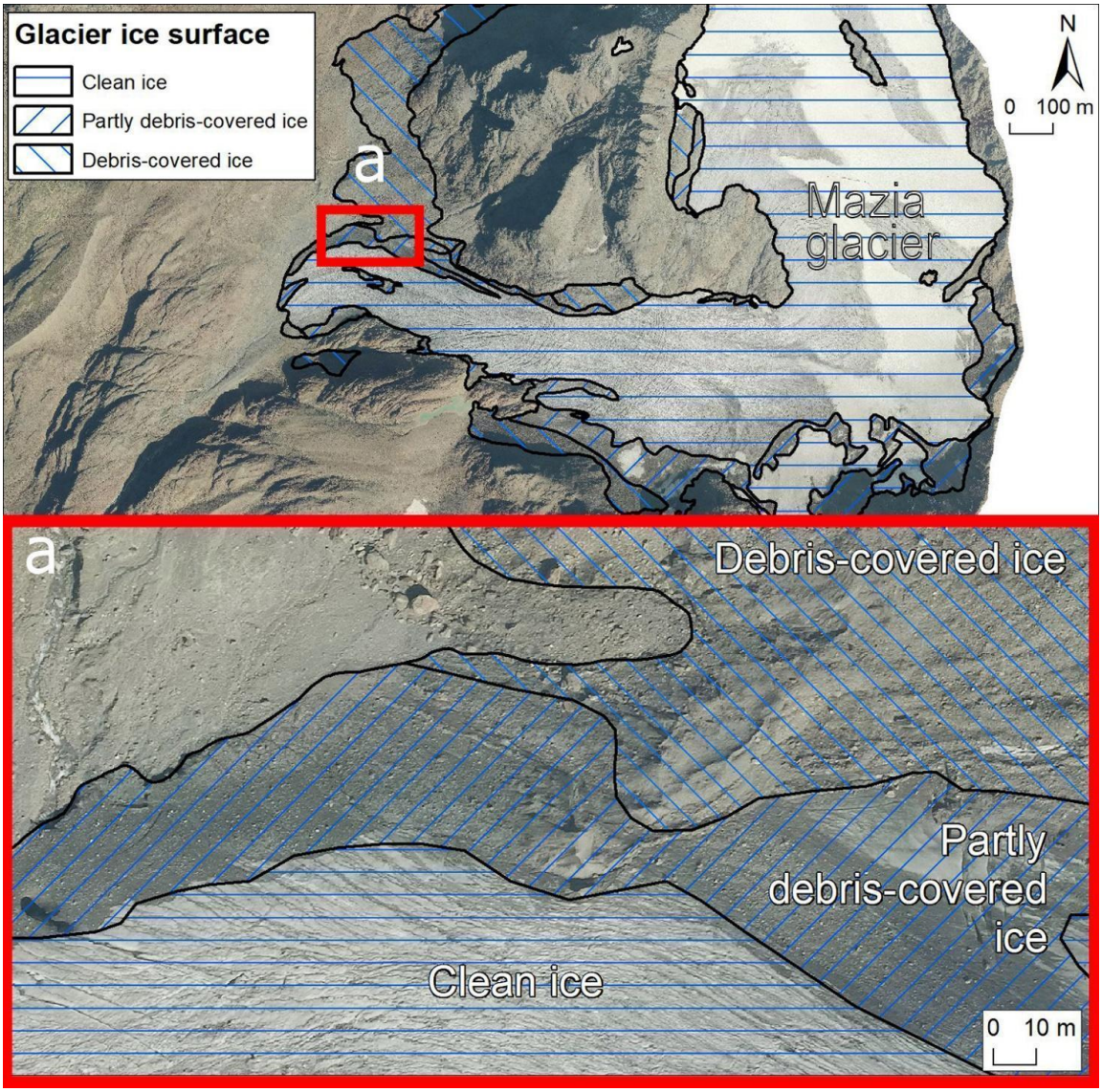

Figure 4. Example of glacier ice mapping following the debris-cover classification scheme.

3.1.2 Geological mapping

The multi-temporal geological mapping relies on the Silandro 1:50,000 CARG mapsheet, which reflects aerial photo interpretation and field surveying finalized in 2006 at a mapping scale of 1:10.000. The new Geological and Geothematic Cartography Project of Italy (CARG Project, CARtografia Geologica) was implemented in 1989 by the Servizio Geologico Nazionale (currently in ISPRA as Dipartimento per il Servizio Geologico d'Italia). The CARG Project is a national initiative that undertakes the compilation and publication of 636 geological mapsheets at the 1:50,000 scale, both in paper and digital format (https://www.isprambiente.gov .it/Media/carg/). The database contains cartographic information on the spatial distribution of bedrock geology, structural features and Quaternary covers. This set of spatially distributed information is critical for land planning, land management, and in particular for the prevention, reduction, and mitigation of hydrogeological risk.

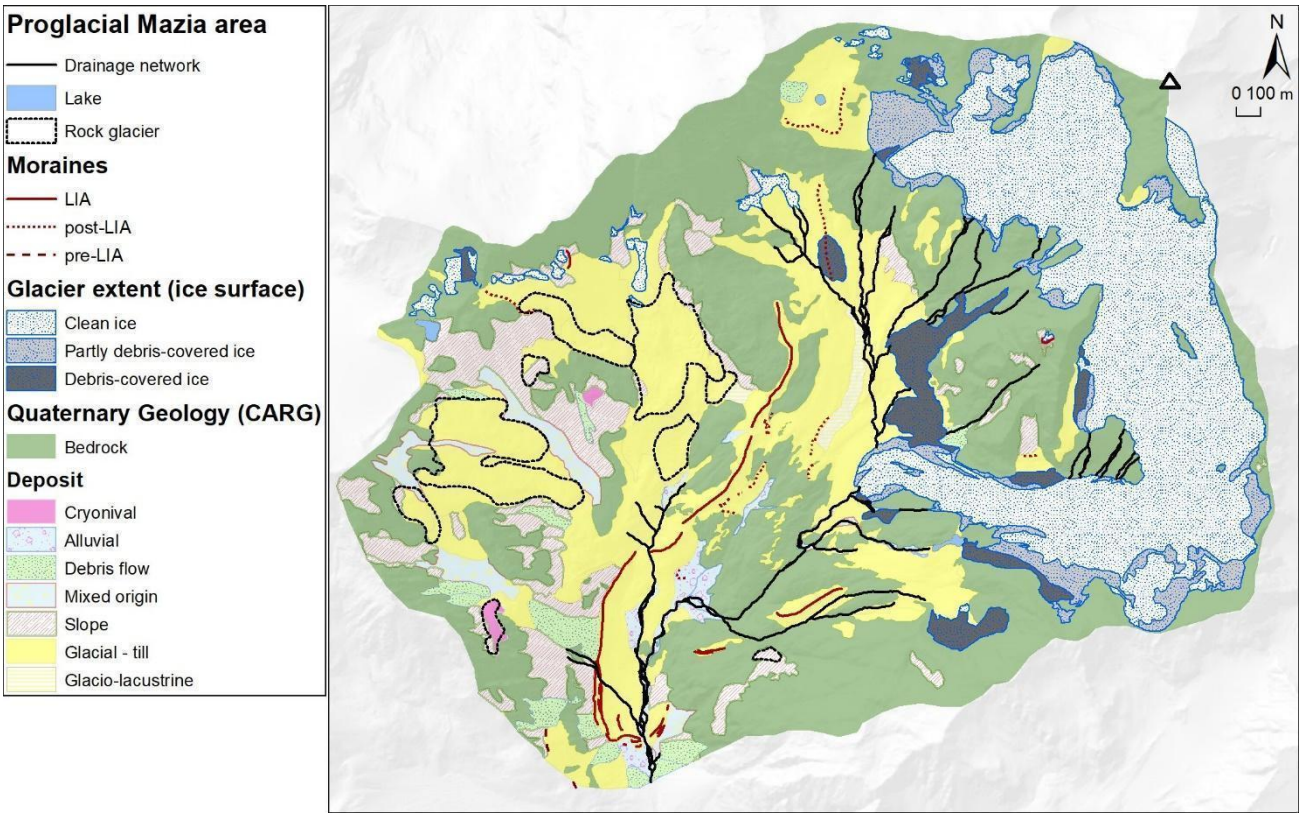

*Figure 5. Sample map of glacier ice surface, outcropping bedrock, Quaternary sedimentary covers, moraine ridges and the drainage network in the Proglacial Mazia area in 2020. The drainage network refers to stream links with visible stream flow at time of imagery acquisition (see **Table 3** for details).*

Following standard procedures customarily conducted by personnel of the Ufficio Geologia and Prove Materiali in Cardano, the original mapping is first conducted and compiled at the 1:10,000 scale; subsequently, 1:10,000 tiles are combined in one mapsheet at the 1.50,000 scale. Given the SedInOut objectives, concerned with the evaluation of glacigenic sediment that becomes exposed during deglaciation and may be remobilized through mass wasting processes and fluvial transport, starting from the original 2006 CARG mapping, special care was taken on refining the mapping of Quaternary surficial materials (**Figure 5)**. In particular, changes to the existing CARG mapping involved increased spatial detail in the delineation of shallow Quaternary covers (i.e., ≤ 1-1.5 m thick), which were originally mapped as bedrock, hence underestimating available sedimentary surfaces (e.g., **Figure 6**). Mapped categories encompass outcropping bedrock, glaciers, and a series of Quaternary materials including glacial, glaciolacustrine, cryonival, slope, debris-flow, alluvial and mixed origin deposits (**Figure 5**). In this context, glaciers are further subdivided according to the three-part debris-cover classification scheme previously introduced (**Table 2**).

Starting from 2006, this Quaternary mapping scheme was applied backward to 1994 and 1969, and forward to 2014, 2016 and 2020 (**Table 1** and

Figure 5 **5**). Mapping involved: (i) visual inspection of sequential aerial photo sets (**Table 1**); and (ii) field surveys in conjunction with the aid of oblique aerial photos taken from helicopter flights. In particular, snow-free conditions in optical imagery from 2016 and 2020 have been critical for identifying shallow glacial deposits (till) (e.g., **Figure 6**).

In the results (**Section 4**), this post-1969 multitemporal mapping will allow evaluating areal changes in bedrock outcrops and Quaternary materials during deglaciation, thereby providing a quantitative assessment of newly available sediment.

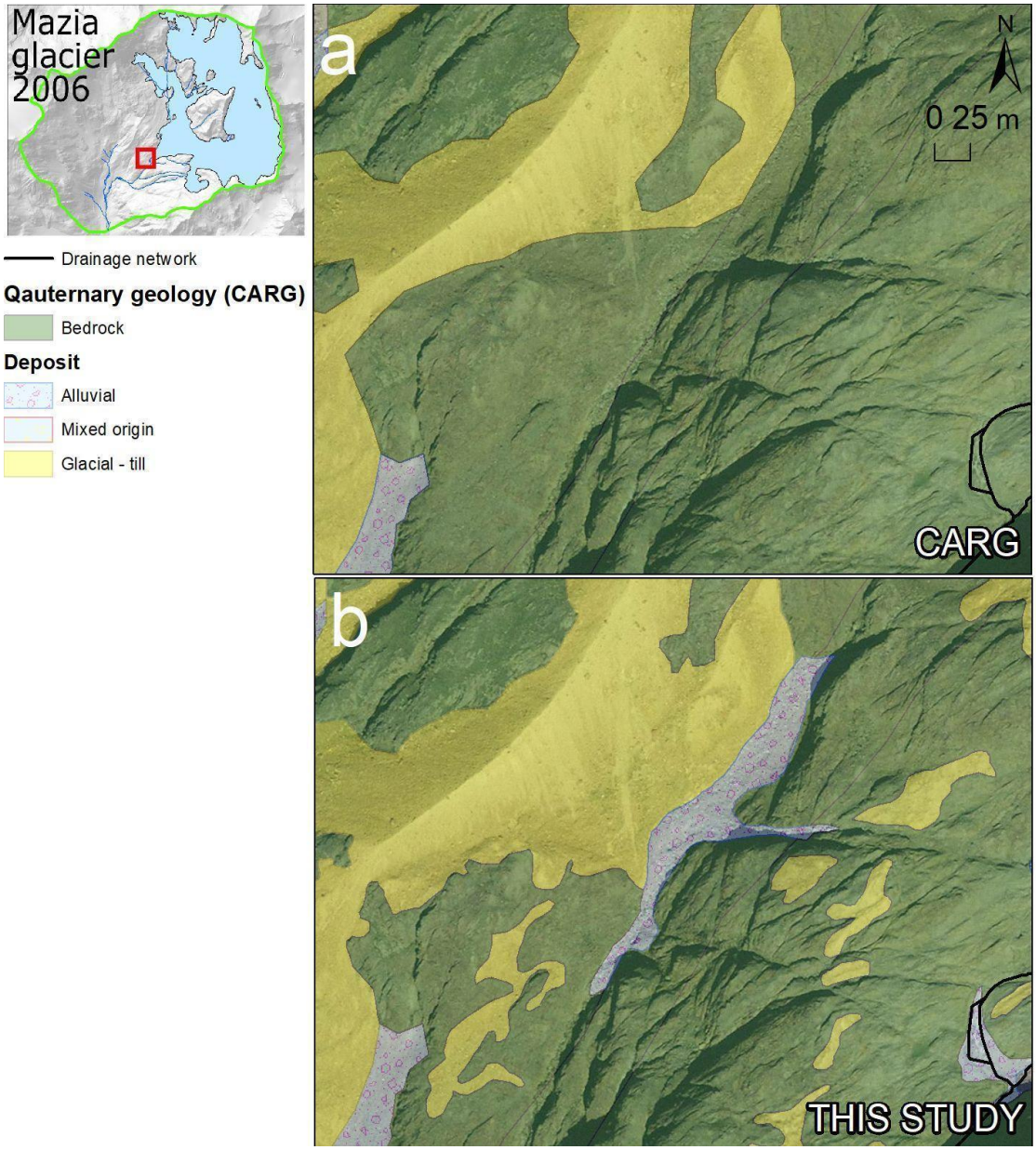

*Figure 6. Example of Quaternary geology and drainage network mapping (photo year 2006) within the Proglacial Mazia Area: (a) original CARG version; and (b) refined version of this study. The drainage network refers to stream links with visible stream flow at time of imagery acquisition (**Table 3**).*

3.1.3 Main drainage network

This multi-temporal mapping component aims to investigate how the main drainage network changes as the Mazia Glacier recedes and fragments into smaller glaciers and patches of buried ice. We are interested in documenting how the main glacier-fed hydrological and sedimentary pathways change during deglaciation. To this purpose, we manually mapped at the scale of 1:500 the portions of the main drainage network bearing perennial stream flow at the end of the summer, across the sequential aerial photo sets (**Table 1**). The selection of historical imagery acquired at the end of the summer allows minimizing uncertainty associated with variable snow cover conditions, and therefore on: (i) bare ground visibility, which affects mapping completeness; and (ii) snowmelt streamflow generation from late spring to midsummer, which would confound identification of glacier-fed stream channels.

To minimize alignment issues across orthophoto sets, the positioning of the mapped drainage network was checked against the synthetic drainage network extracted from three high-resolution gridded DEMs acquired in: (i) 2006 (5-m cell; airborne LiDAR); (ii) 2013 (0.5-m cell; airborne LiDAR); and (iii) 2016 (0.5-m cell; airborne photogrammetry). Following historical glacier changes it was then possible to document the structural evolution of the drainage network in progressively de-glaciated areas (**Figure 7**). To aid distinguishing between surface and subsurface hydro-sedimentary pathways, we classify the network links into four categories, depending on stream flow visibility. Categories include links where stream flow is: (i) *visible*; (ii) *partly visible*, due to spatial interruptions associated with water loss to subsurface; (iii) *intermittently visible* (or subnival/subglacial), with stream flow intermittently hidden by small perennial or seasonal snow-fields, or by patches of buried ice; and (iv) *not visible*, when visible lakes/ponds and/or ice patches are connected to the main perennial drainage network through subsurface flow along well-defined deglacial, debris-choked channel segments (see **Table 3** for definitions). Through the photo years, channel segments that become disconnected from the receding Mazia glacier and therefore do not exhibit perennial stream flow, are trimmed off the mapped drainage network (e.g., **Figure 7**).

Stream flow	Description
Visible	Segments where stream flow is clearly visible at the scale of 1:500.
Partly visible	Segments with visible stream flow characterized by short and frequent interruptions associated with infiltration loss under the debris cover.
Intermittently visible (subglacial)	Segments with stream flow intermittently hidden in time by small perennial or seasonal snowfields, or by glacier portions. The channel bed is clearly visible in photo years bearing snow or ice-free conditions.
Not visible (subsurface)	Segments with no surficial stream flow connecting visible sources of freshwater, including snow/ice patches and lakes/ponds (upper end), to visible perennial stream channels (lower end). Connection occurs through subsurface flow along well-defined deglacial, debris-choked channel segments.

Table 3. Classification of the drainage network with respect to end-of-summer stream flow visibility.

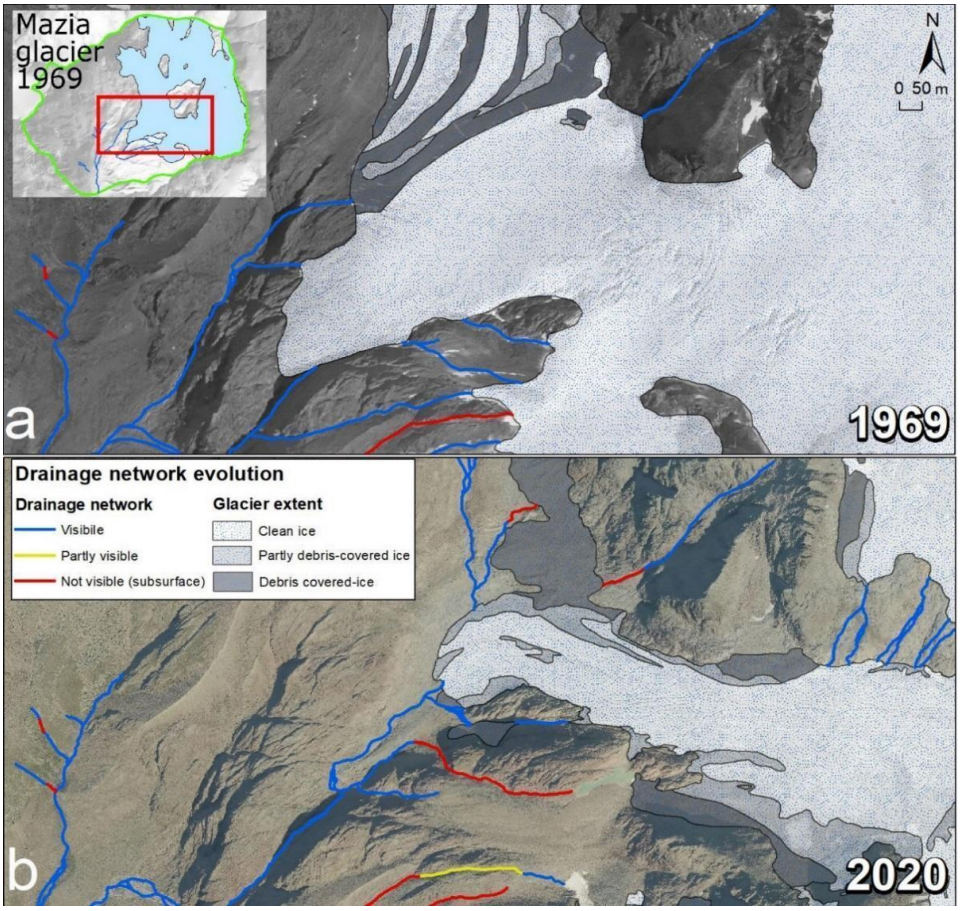

*Figure 7. Sample view showing the drainage network configuration in proximity of the Mazia Glacier front in photo years 1969 and 2020. Color-coded segments follow the classification scheme outlined in **Table 3.***

3.1.4 Rapid shallow landslides

The multi-temporal inventory aims to evaluate in what proportion sediment mobilized by rapid shallow landslides (hereafter termed landslides for simplicity) in Mid and Upper Mazia Valley is delivered to ephemeral and perennial stream channels. This database, built from a landslide inventory (1959-2008) that was originally compiled in the context of the Alpine Space SedAlp project (www.sedalp.eu), has been revised and updated to photo-year 2020. Compilation and revision have entailed stereoscopic inspection of two sequential aerial photosets (1959 and 1969) and six orthophoto mosaics (1982/85, 1997/99, 2006/08, 2011, 2015, and 2020) (**Table 1**).

In the database, each landslide track is characterized by a set of attributes including: (i) photoset of first detection; (ii) activity through sequential photosets; (iii) movement type; (iv) morphology at initiation site; and (v) sediment delivery site. The last attribute is extremely relevant to SedInOut, as it allows assigning to each landslide a sediment delivery potential to perennial streams (**Table 4**). This scheme – first developed by Maynard (1991) in coastal British Columbia, and subsequently adapted to high-elevation, crystalline glaciated settings (Brardinoni et al., 2015) – classifies landslides into three broad categories. Accordingly, delivery potential to perennial streams is regarded as: (i) low, when a landslide delivers sediment to unchannelled topography (e.g., hillslopes, talus cones and moraine ridges); (ii) moderate, when landslide sediment reaches seasonal/ephemeral channels (here termed gully channels) and transitional sedimentary linkages (e.g., alluvial and debris-flow fans); and (iii) high, when landslide sediment enters directly the perennial drainage network (**Table 4**).

During aerial photo interpretation (API) we have identified two main types of shallow rapid failures: debris slides (ds), and channelized debris flows (dsdf) (Hungr, 2005, 2014). After identification, the outline of the total disturbed area associated with each landslide track has been manually digitized in GIS environment so that a series of planimetric attributes on landslide geometry could be extracted. These include landslide length, width, and area. Subsequently, to provide a first-order approximation of the area associated with landslide-derived debris and avoid overestimation, following the specifics described by Brardinoni et al. (2009), each track has been subdivided into: (i) initiation and transportation zones - down to the point where scouring is manifestly visible - and (ii) deposition zone, where signs of deposition become evident. Once planform areas of initiation/transport and deposition zones are obtained, volumetric estimation

of mobilized debris is made by applying to either initiation/transport or to deposition areas a field-based area-volume relation (**Section 3.2.1**).

UNCHANNELED TOPOGRAPHY:	**(s) slope**
(on-site, low deliverability)	**(ts) talus slope**
	(tc) talus cone
	(rg) rock glacier
	(m) moraine
	(kt) kame terrace (glaciofluvial)
SEASONAL CHANNELS & TRANSITIONS:	
(moderate deliverability)	**(f) fan**
	(gc) gully channel (ephemeral channel)
	(cg) connected gully channel (directly connected to a perennial channel)
	(r) road
	(ft) fluvial terrace
	(fp) floodplain
	(lk) lake or reservoir (permanent freshwater sink)
PERENNIAL CHANNELS:	**(mc) main channel (river mainstem)**
(high deliverability)	**(ct) connected tributary (perennial tributary connected to the river mainstem)**
	(ut) unconnected tributary (connected to another tributary and not directly connected to the river mainstem)

Table 4. Landslide sediment deliverability (or delivery potential) to perennial stream channels. Bold text marks delivery sites found in Mazia Valley.

3.2 Field and proximal sensing techniques

3.2.1 Geometry of shallow rapid failures

API-derived data are complemented by a field-based inventory that comprises 113 landslide tracks. During field data collection, landslide planimetric shape was approximated to a rectangle, so that landslide area is derived by multiplying landslide average width by landslide length. Landslide volume was estimated by multiplying landslide area by landslide track thickness. These geometric variables were measured by a team of two surveyors with a stadia rod and a metric tape, and in the case of particularly long scars, by means of a laser range finder. Measurements on landslide geometry are performed to constrain an empirical field-based, landslide area-volume relation (e.g., Guzzetti et al., 2009). This relation is then used to translate API-based landslide areas (e.g., **Section 3.1.4**) into volumes of mobilized debris. Considering the higher uncertainty associated with the identification and temporal classification of landslide initiation and transportation zones, in our analysis we have decided to adopt a conservative approach, thus have considered the API-based areas of landslide deposits only.

3.2.2 Characterization of channel bed texture and armouring

Characterization of surface and subsurface grain-size distributions has been conducted at six sites (**Figure 2a**), selected to represent typical geomorphic conditions within the glaciated landscape of Upper Mazia Valley. In particular, we have sampled the course of the main Saldur Creek (Rio Saldura) and that of two contrasting lateral tributaries: Oberettes Creek, originating from the remnants of a debris-covered glacier, and on the opposite valley side, an unnamed tributary, originating from an active rock glacier (**Figure 8**). In Saldur Creek, we started sampling at the glacier front, on plane-bed channel morphology that characterizes the hanging floodplain of the Mazia glacier forefield (site M1). We then proceeded to multi-thread reaches past the valley step at the beginning of the main Mazia glacial through, by the LIA moraine (site M2), and continued further downstream in proximity of the two contrasting lateral tributaries (site M5). In Oberettes Creek, we have sampled bars of the hanging braided floodplain partly dammed by a LIA moraine (site M2) and continued past a sub-vertical valley step (bedrock gorge) and down to the steep debris-flow fan by the confluence with Saldur Creek (site M4). Finally, in the unnamed tributary opposite to Oberettes, which originates from a rock glacier and flows mostly to subsurface

through a series of well-preserved Lateglacial lateral moraines, we have sampled the distal portion of the small alluvial fan by the confluence with Saldur Creek (site M6).

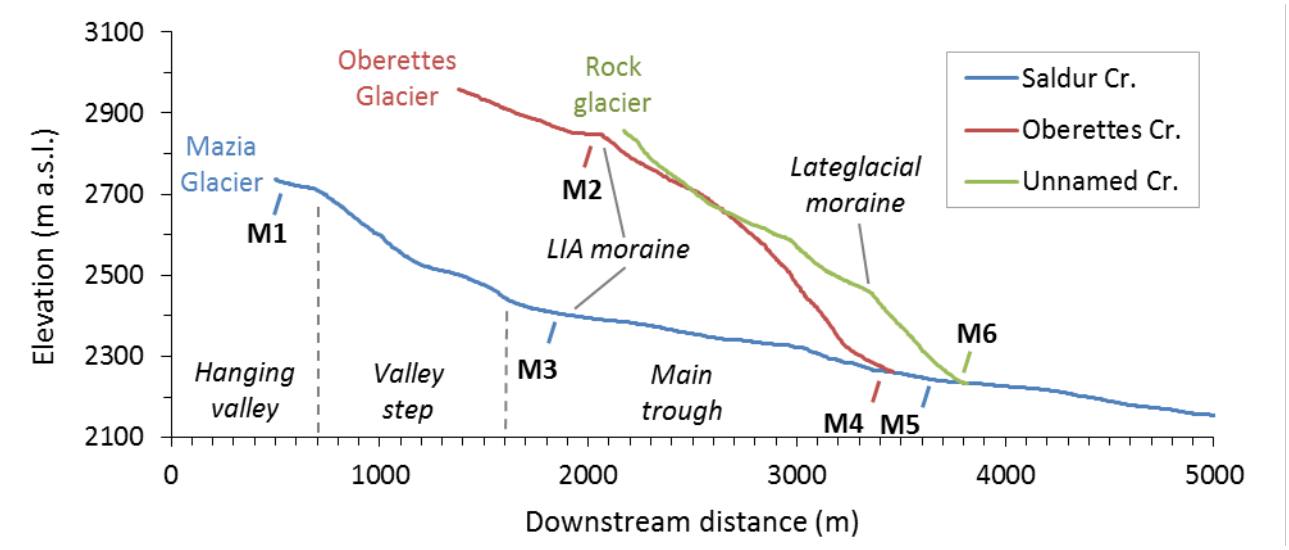

Figure 8. Location of the sediment sampling sites (i.e., M1 through M6) across the longitudinal profiles of Upper Saldur Creek (blue linework) and the tributaries Oberettes Creek (red linework) and Unnamed Creek (green linework). The long profiles start respectively at the Mazia glacier front, at the Oberettes glacier front, and at an active rock glacier front.

The methodological workflow integrates field, laboratory, and proximal sensing techniques (**Figure 9**). We started from selecting representative channel bars at strategic sites of the channel network across the Upper Mazia Valley. Surface grain-size distribution (GSD) was then characterized in two independent ways, by means of: (i) Wolman pebble count ($n \geq 250$) conducted across the bar surface (Wolman, 1954); and (ii) GrainID, a CNN-based model of image analysis of close-range vertical photos taken in the field (Chen et al., 2022). The former method generates grid-by-number surface GSDs (Kellerhals and Bray, 1971). The latter, which is performed by combining 1m x 1m photo tiles taken at representative facies locations across the channel bar produces grid-by-area surface GSDs of all grains detected on the imaged channel bed. As a further means of comparison, surface GSD was also performed on the same set of close-range vertical photos through manual labeling of single clasts, which was then followed by BASEGRAIN post-processing (Detert and Weitbrecht, 2012; 2013). For each photo tile, BASEGRAIN produces a grid-by-area GSD based on a line sampling approach, i.e., the b-axes of all grains that are in contact with a line drawn across the photo, are measured.

Subsurface GSD characterization was conducted via removal of the surface sedimentary layer at one of the tile locations followed by bulk sampling of the subsurface material. Subsequently, the coarse fraction (≥ 64 mm) was mechanically sieved and weighed on-site. The remainder (finer)

portion of the sample was carried to a base camp by helicopter, and then transported to the lab in Cardano by truck for further mechanical sieving.

It is important to highlight that in all sieving methodologies (i.e., on-site and laboratory mechanical sieving, manual sieving of single clasts through Wolman pebble count, and photo sieving on close-range vertical photo tiles) the intermediate axis (i.e., b-axis) represents the limiting dimension for a clast to pass or be retained through a mesh of a given size. Consequently, photo sieving conducted on imbricated of even weakly tilted clasts (i.e., the a and b axes are not imaged orthogonally to the photo camera) involves some degree of b-axis underestimation (e.g., Church et al., 1987). In the worst case-scenario, imbrication might imply that through photo sieving one is indeed measuring the size of the c axis, as opposed to the b counterpart (cf., **Section 4.5**).

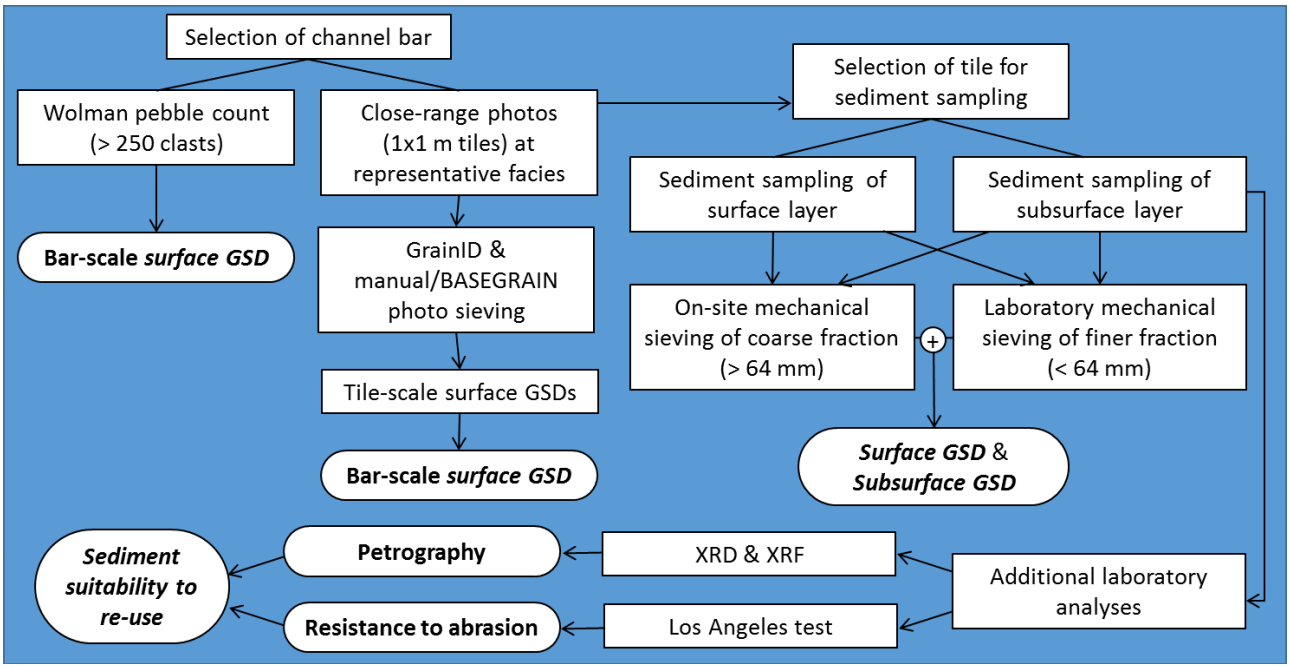

Figure 9. Methodological workflow adopted for characterizing surface and subsurface grain-size distribution (GSD), as well as laboratory analyses for evaluating sediment suitability to possible re-use.

3.2.2.1 Close-range vertical photo collection and photo sieving (surface GSD)

Exploratory automated photo sieving, manual delineation of grains and BASEGRAIN processing

After selection of a representative channel bar, a series of vertical, close-range (i.e., from 1 m above the ground) photos of the bar surface are taken. Each photo is then cut down to a 1x1 m tile. In Mazia Valley, the number of photo tiles varies from 5 to 12, depending on bar size and complexity. Collectively, the photo tiles are meant to capture the longitudinal variability in surface bed texture from bar head to bar tail.

At an exploratory level, we first ran automated photo sieving procedures to the photo tiles by means of three softwares: (i) JMicroVision (Roduit, 2008); (ii) ImageJ (Arganda-Carreras, 2008); and (iii) BASEGRAIN (Detert and Weitbrecht, 2012; 2013) **(Figure 10**). Following these tests, we found that automated photo sieving involved time-consuming operations associated with the fine-tuning of image parameters, and that ultimately this did not yield consistently reliable clast recognition outputs across different photo tiles. Obvious misclassifications were associated with variable lithology, clast angularity, and occurrence of fine-grained materials (cf. **Section 4.5**). Consequently, we decided to proceed with the manual delineation of each clast that was assuredly identified through visual inspection of each photo tile. This is a time-consuming approach, which however will yield more consistent results across photo tiles. After manual delineation, each photo tile was processed through BASEGRAIN (**Figure 11).**

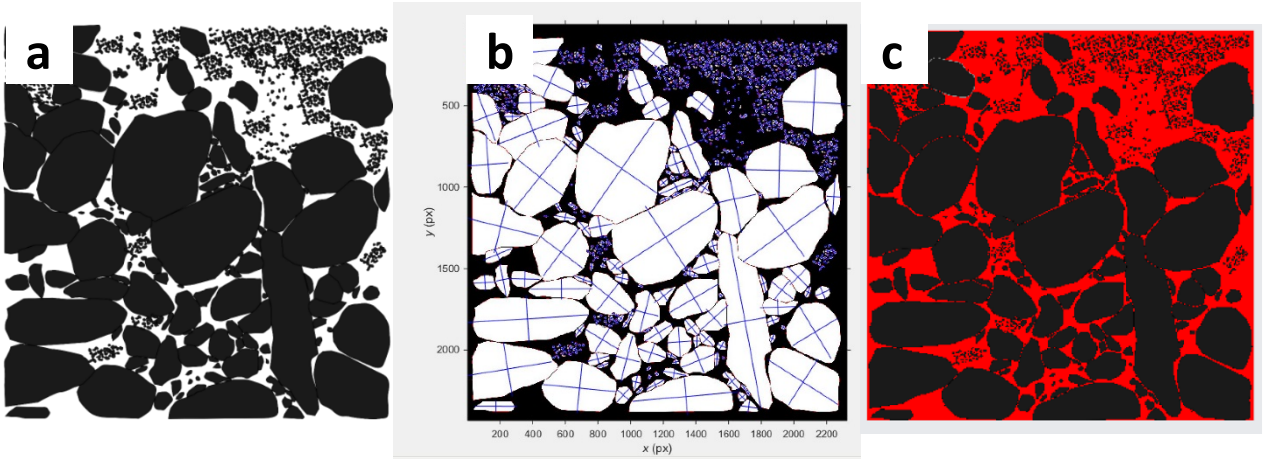

Figure 10. Sample photo tiles as classified through application of: (a) JMicroVision; (b) ImageJ; and (c) BASEGRAIN. Results obtained after manual delineation of the clasts.

.

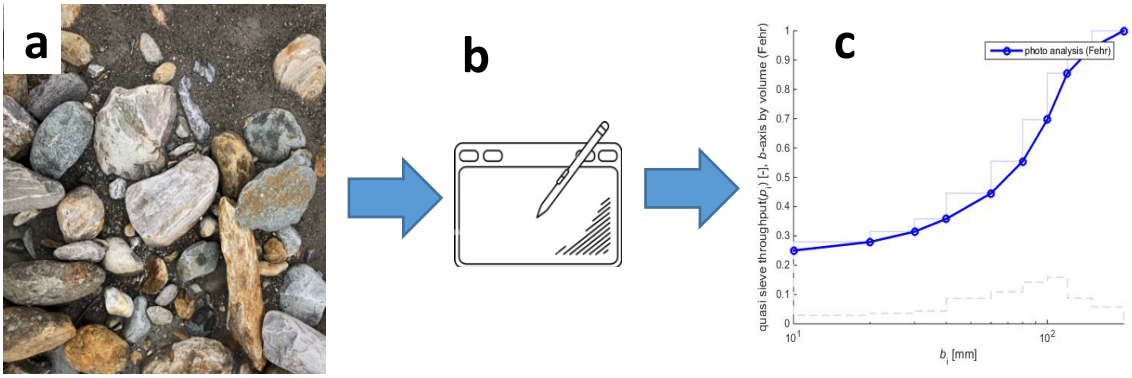

Figure 11. (a) Close-range digital photo; (b) Manual delineations of clasts; and (c) BASEGRAIN-derived surface grain-size distribution.

GrainID photo sieving

To provide an additional independent means of surface GSD characterization, we finally run GrainID (Chen et al., 2022) on the original photo tiles. GrainID is a model framework based on convolutional neural networks that measures grain size in optical images taken across diverse fluvial environments. The model is developed in Python and is freely available. GrainID structure is summarized in **Table 5.**

Procedures	Operation	Description
Step 1: Pre-processing	1.1 – image extrapolation-1	If the size (e.g., 2000 × 2000) of original input image could not be equally split into multiple 512 × 512 tiles, the image was extrapolated into 2048 × 2048 based on mirroring the right and down image border region.
	1.2 – image extrapolation-2	Based on the overlap-tiles strategy, for prediction of image border region, the missing context was extrapolated by mirroring the border region.
	1.3 – contrast filter	A sigmoid contrast filter in Python library Pillow was applied.
	1.4 – image augmentation	The input images were augmented by applying 0, 90 and 180° counterclockwise (CCW) rotation and horizontal and vertical flip.
	1.5 – image split	Input images were split into overlapping image tiles (512 × 512) as dashed red and blue rectangles in Fig. 4b.
Step 2: Prediction	2.1 – U-Net prediction	All image tiles were then sequentially input into U-Net for prediction.
	2.2 – recombination	The predicted image tiles were recombined into a full image.
	2.3 – assemble vote	The final CNN prediction was calculated as an image assembly decided by predictions from the five augmented images.
Step 3: Post-processing	3.1 – filling holes	The holes inside grains were filled.
	3.2 – filter fine grain	Unresolvable grains with size < 20 pixels were deleted.
	3.3 – narrowing interstice	An inverse watershed algorithm was applied.
	3.4 – watershed algorithm	A watershed algorithm was performed for further separation.

Table 5. Image processing steps composing the GrainID model framework (from Chen et al., 2022).

3.2.2.2 Sample collection for surface and subsurface GSD characterization

Surface GSD

For selected sites, after identification of a representative channel bar, we characterized surface grain-size distribution in two field-based independent ways: (i) Wolman pebble count (Wolman, 1954), through a random walk approach (see Kondolf et al., 2003 for details) consisting in the measurement of the b-axis of at least 250 clasts (**Figure 12a)**; and (ii) Bulk sample collection of the surface layer within 1x1 m tiles, followed by on-site sieving of the coarse fraction (> 64mm, **Figure 12b**) and laboratory sieving of the finer material.

Subsurface GSD

Bulk sampling and sieving

After removal of the surface layer (i.e., down to a depth of 2 x D90 established through Wolman pebble count), the procedure involved:

(i) on-site preliminary mechanical sieving of the coarse subsurface material (> 64 mm), up to 70 kg per sampling site, depending on the sorting of the relevant sediment mixture.

(ii) sample collection of the remaining finer fractions, which were carried to the Cardano rock laboratory (about 40 kg per site) for further sieving.

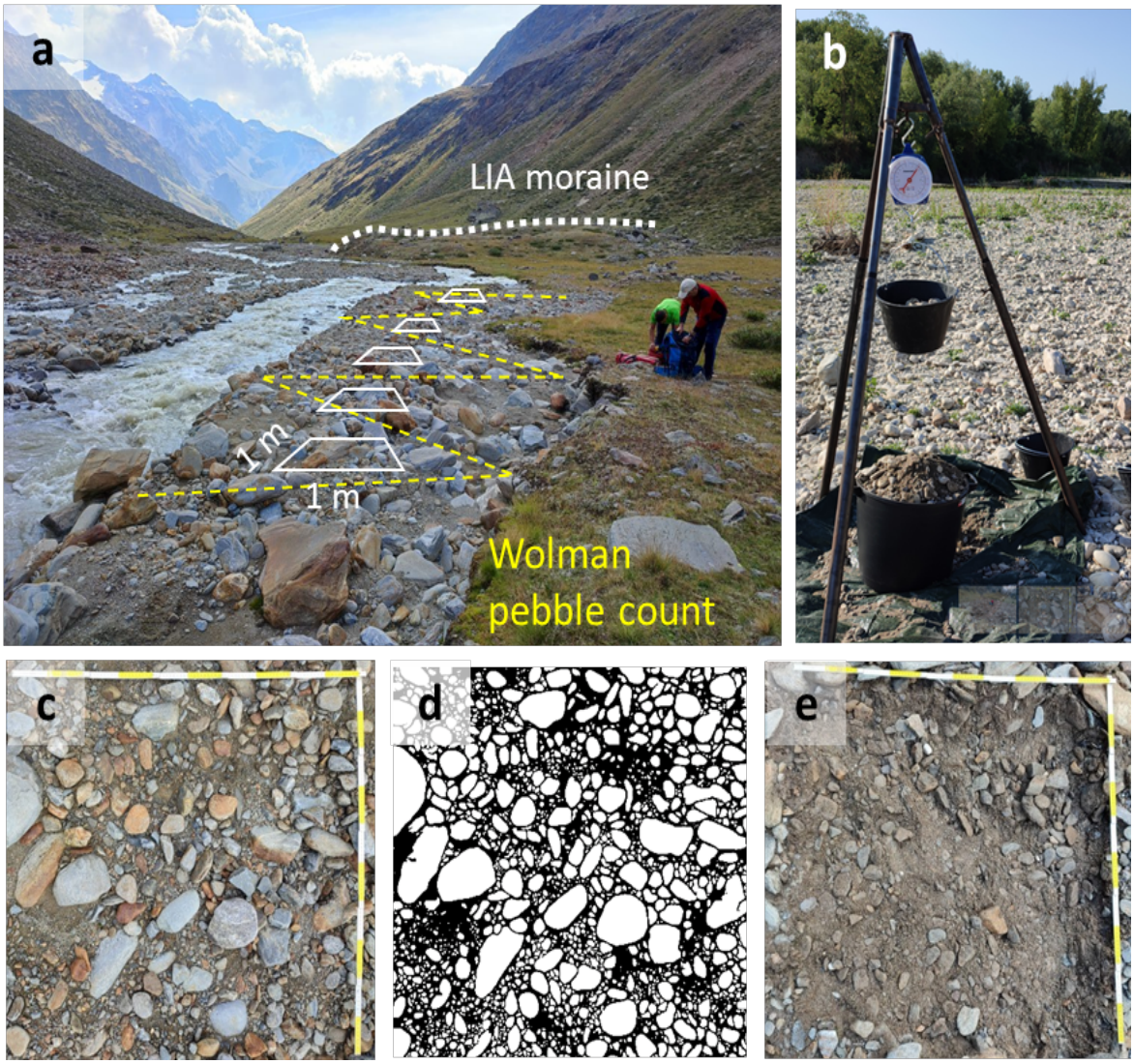

Figure 12. Some of the methodological steps involved in the GSD characterization, illustrated for sampling site M3 in Upper Mazia Valley. (a) Random walk, Wolman pebble count to obtain bar-scale surface GSD (dashed yellow linework) and siting of 1x1 m sampling tiles (white empty polygons) at representative facies within the lateral bar. (b) On-site mechanical sieving of the coarse sediment fraction (>64 mm) to obtain tile-scale surface GSD and subsurface GSD. (c) Close-range vertical photo of 1x1 tile, (d) relevant output derived from Grain-ID photo sieving, and (e) close-range vertical photo after removal of the surface layer. In panel a, thick dotted linework outlines the ridge of the Little Ice Age moraine. Locations of the random walk path and 1x1m tiles are hypothetical, here sketched for illustrative purposes only.

3.3 Laboratory methods

3.3.1 Mechanical sieving

The steps leading to GSD characterization based on mechanical sieving of the field sediment samples were conducted in the rock laboratory of the Office of Geology and Materials Testing in Cardano. These involved: (i) sample weighing before heating; (ii) sample heating in the oven at 105°C for water content removal; (iii) sample weighing after heating (i.e., following UNI EN-933-1 norm: about 40 kg each, with maximum grain diameter of 90 mm; (iv) sample washing through a coarse sieve and down to a fine sieve to separate the finest fractions (i.e., <0.0063 mm) from the rest; (v) sample heated again at 105°C; (vi) the washed and dried sample is weighed to determine the percentage of fines (<0.0063 mm); (vii) mechanical sieving through a sieve tower and subsequent weighing of the sieved fractions. In particular, the tower consists of 17 meshes and separates the following grain size fractions (expressed in mm): 90, 64, 56, 45, 32, 22.6, 16, 11.3, 8, 5.6, 4, 2, 1, 0.5, 0.25, 0.125, 0.063, < 0.063 (**Figure 13**).

Figure 13. Examples of retained sediment fractions after mechanical sieving.

3.3.2 XRD analysis

To support the petrographic (and geochemical) analysis, we applied the X-Ray Diffraction (XRD) method in the rock laboratory of the Office of Geology and Materials Testing in Cardano. The XRD method consists of the calculation of the diffraction angle of the material that is beamed by X-ray transmission. This method is suitable for providing a semiquantitative analysis containing the mineralogic composition of a rock sample. The analysis of petrographic specimens has been conducted on samples from project partner 2 (Regione Friuli-Venezia-Giulia) that have been retrieved in the Rio Fella and Rio Cucco basins. Due to homogeneous lithologic composition (i.e., micaschist/paragneiss) and previous petrographic analysis of the main rock types (thin sections) these analyses have not been conducted in Mazia Valley.

3.3.3 Los Angeles Abrasion Test

The Los Angeles Abrasion test (LAA) reflects the aggregate resistance to abrasion and fragmentation due to impact. The test measures the resistance of aggregate to wear due to attrition between rock particles and to impact and crushing by steel spheres (Ugur et al., 2010). The sample to be tested is placed together with 6-12 steel beads in a steel drum that rotates 500 times around its own axis and crushes the test material by abrasion and impact stress. Within the aims of the SedInOut project the LG 02.12-UNI EN 1097-2 norm was implemented. The procedure consists of six working steps including: (1) sample dry weighing; (2) sample washing; (3) additional weighing of washed sampled; (4) grain fraction separation through tower sieving; (5) sample tumbling in LA machine; and (6) LA-test outputs.

3.4 Grain size outputs

The grain size distribution of channel bed material is characterized for a range of purposes in sedimentology, geomorphology, hydraulic engineering, and freshwater ecology. Among a wide spectrum of applications, this quantitative information may be used as input for bedload transport equations to evaluate bed mobilization and likelihood of scour, as a measure of grain roughness, as one of the means to assess sediment suitability for use (or re-use) in construction works.

In this study, channel bed data outputs at each sampling site include (**Figure 14)**:
(i) the surficial grain size distribution obtained by means of field-based Wolman pebble counts (hereafter termed Wolman) and through GrainID convolutional neural network processing of close-range vertical photos (hereafter termed GrainID; Chen et al 2022);

(ii) subsurface grain size distribution obtained solely through laboratory mechanical sieving of the finer fractions (≤ 64 mm) (hereafter termed Lab) and that obtained through integration of on-site sieving of the coarser fractions (hereafter termed Field & Lab).

From these surface and subsurface grain size distributions were derived characteristic sediment percentiles (Di) including D50, D84 and D90. The so-called surface D50, the median sediment caliber of an active channel bar, represents a measure of central tendency of the sediment mixture and indicates which calibers move during the most frequently recurring flows associated with bankfull. Surface D84 and D90 (or Dmax) are a proxy of grain resistance to flow (in ordinary flow conditions) and geo-hazard potential due to channel instability and catastrophic runout that would involve the mobilization of such coarse calibers. Finally, the armour ratio is derived (i.e., the ratio between surface D50 and subsurface D50), which represents a measure of both channel stability and sediment supply (e.g., Gomez, 1983; Hassan et al., 2006; 2020; Hassan and Zimmermann, 2012). Accordingly, a ratio larger than unity indicates that an armour layer has developed. At a given channel location, the higher the armour ratio the more effective this shielding will be against bed surface destabilization during floods.

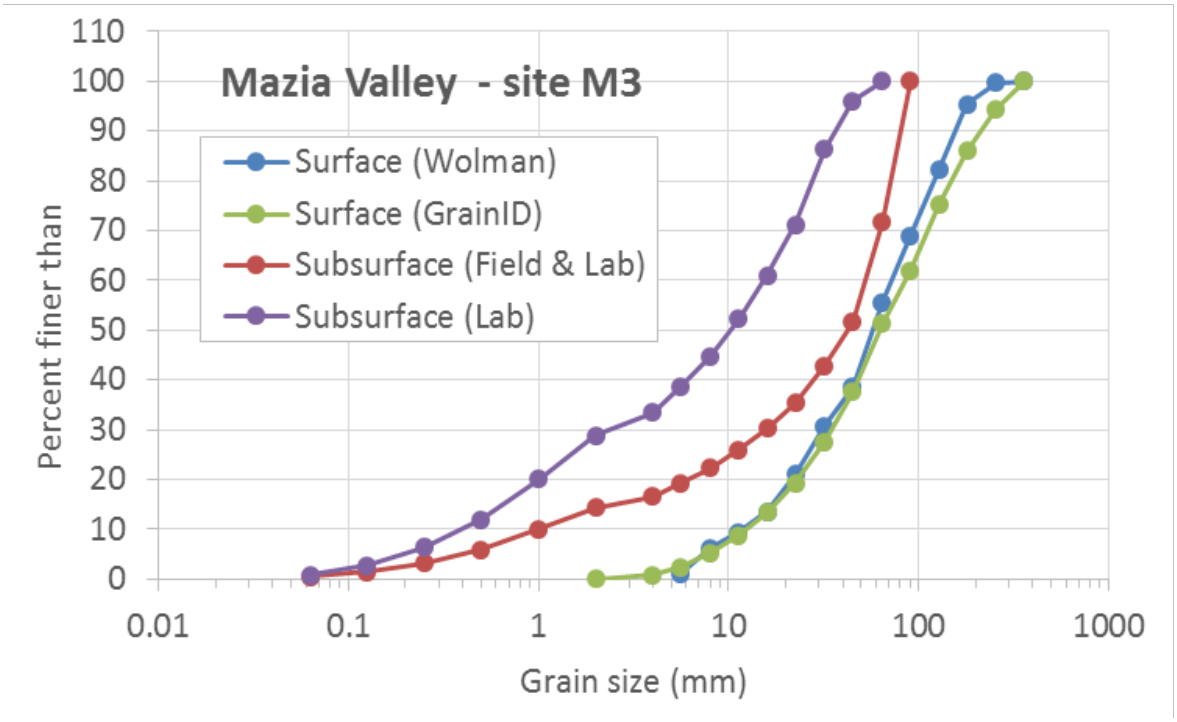

Figure 14. Example of surface and subsurface grain size distributions (GSDs): sampling site M3. The Wolman-based surface GSD (blue linework) derives from the collection and measurement of 250 clasts (blue linework). The GrainID-based surface GSD (green linework) derives from the analysis and amalgamation of five 1x1 m tiles distributed at representative facies locations across the lateral bar M3. The subsurface GSD derives from the preliminary on-site mechanical sieving of the coarse fraction (> 64mm) (violet linework) in conjunction with the finer counterpart (< 64 mm) sieved in the laboratory (red linework).

4. Results

4.1 Glacier retreat, increase in outcropping bedrock and glaciogenic sedimentary surfaces, and evolution of the glacier-fed drainage network between 1969 and 2020

Between 1969 and 2020, glacier area in Upper Mazia experienced a reduction of 42.87 %, from 3.76 km^2 to 2.15 km^2 (**Table 6** and **Figure 15**), for an average annual loss of 3.16 ha/yr. Through the photo years examined, loss involved chiefly clean ice (both in terms of absolute and percent area), whereas partly and fully debris-covered ice have witnessed collectively a relative areal increase – from 5% in 1969 to 24% in 2020 – mainly associated with glacier fragmentation that involves an increase of isolated patches of buried (debris-covered) ice. These findings indicate that retreating glaciers in Upper Mazia Valley are associated with a progressively higher load of debris, which is deposited on the relevant forefields for further subaerial reworking.

As glaciers retreat, they uncover bedrock and glaciogenic materials, which progressively become available for mass movements and fluvial transport. During deglaciation, in the Mazia Proglacial area between 1969 and 2020 major land cover changes involve areal increase in bedrock outcrops (from 2.37 km^2 to 3.25 km^2), glacial till (from 1.34 km^2 to 1.97 km^2), and, to a lesser extent slope deposits, whereas the other Quaternary covers remain relatively marginal (**Figure 16** and **Table 7**). Interestingly, the increase in bedrock and till-mantled areas appear to accelerate through time, especially until 2011 (**Figure 17**). Increased bedrock surface may affect peak flow during rainstorm events, hence promoting the occurrence of possible flash floods. Increased till-mantled areas, depending on their location with respect to the main drainage network, may favour increased landslide activity and delivery to streams (see **Section 4.2**).

	Area (km²)					
Photo year	**1969**	**1994**	**2006**	**2014**	**2017**	**2020**
Clean ice (%)	3.5 (95.4)	2.80 (83.7)	2.17 (75.6)	1.92 (80.2)	1.76 (75.9)	1.63 (76.0)
Partly debris-covered ice (%)	0.04 (1.0)	0.18 (5.5)	0.35 (12.2)	0.21 (8.6)	0.31 (13.3)	0.30 (13.8)
Debris-covered ice (%)	0.14 (3.6)	0.36 (10.9)	0.35 (12.3)	0.27 (11.3)	0.25 (10.8)	0.22 (10.2)
Combined	3.76	3.35	2.88	2.39	2.32	2.15

Table 6. Post-1969 glacier area change, stratified by debris cover extent. Numbers in brackets indicate percent area extent within the Upper Mazia Valley.

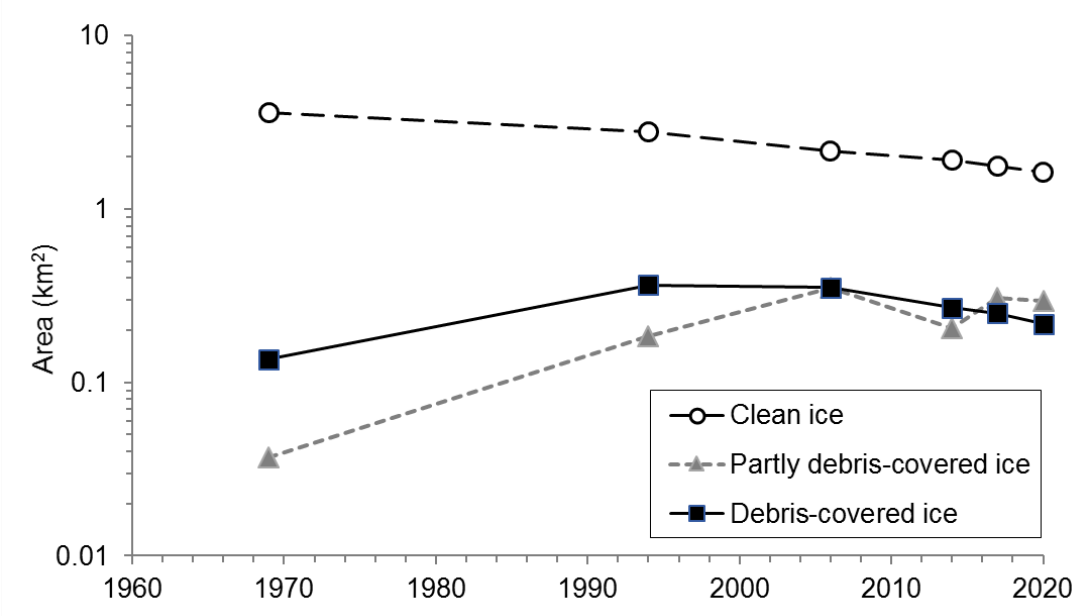

Figure 15. Evolution of glacier area change between 1969 and 2020 stratified by degree of debris cover.

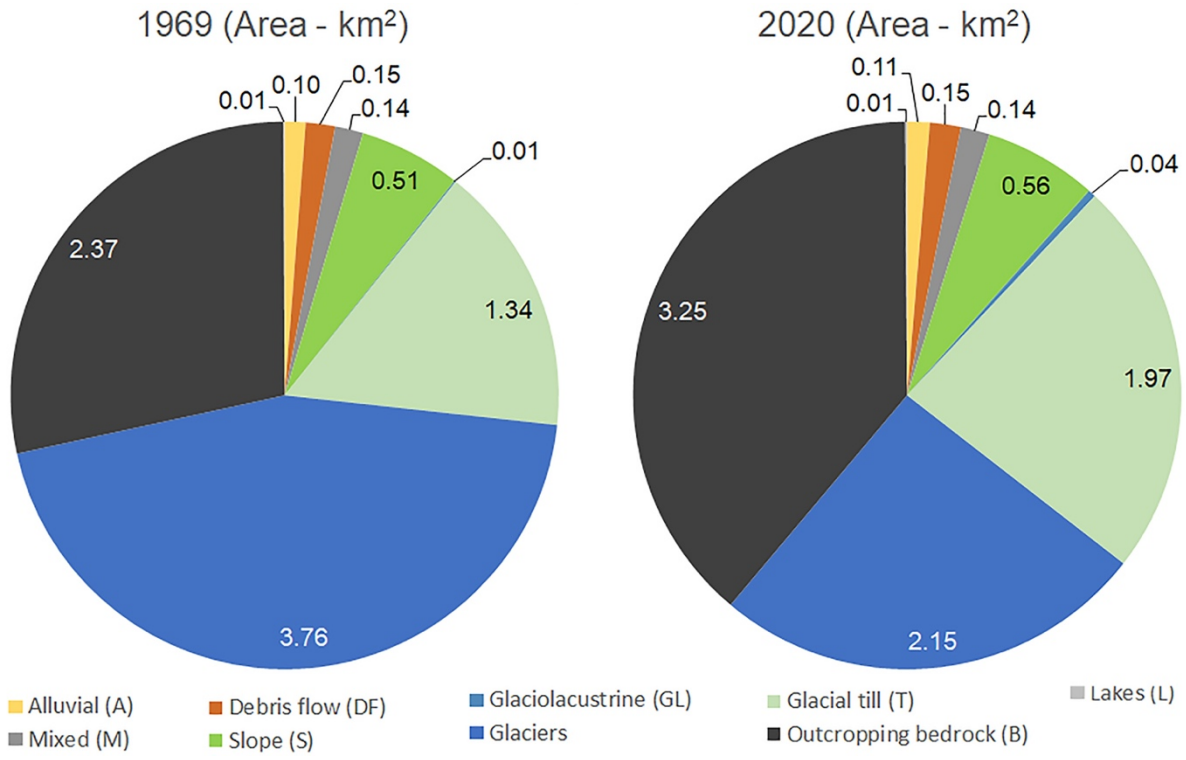

Figure 16.Evolution of Quaternary sedimentary covers, outcropping bedrock and glacier extent between 1969 and 2020.

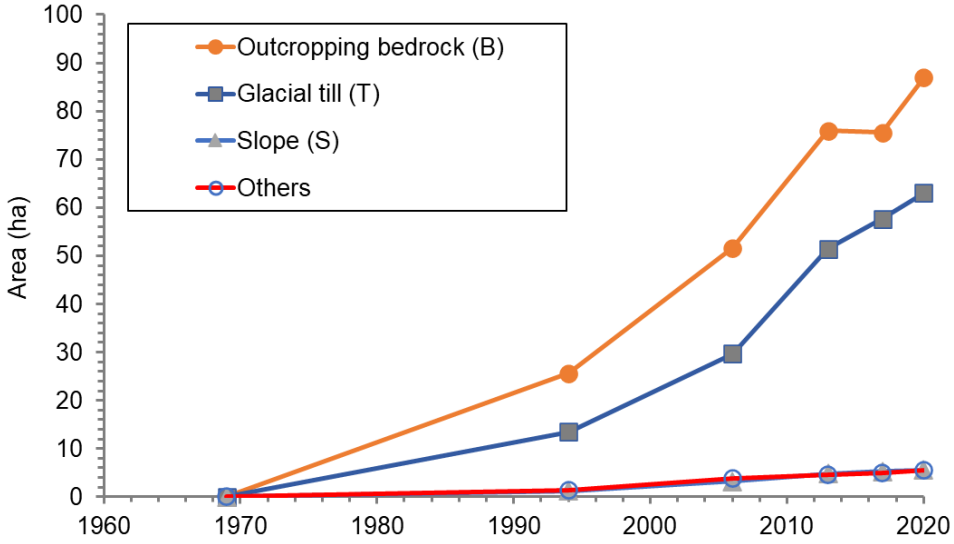

Figure 17. Evolution of outcropping bedrock, glacial till, slope deposits and all other Quaternary covers (i.e., others) during deglaciation within the 1969 glacier footprint (see Table 4.3 for details). Note complete overlap between the area-based functions of "slope"deposits and "others".

	Area (ha)					
Quaternary deposits	**1969**	**1994**	**2006**	**2013**	**2017**	**2020**
Alluvial (A)		0.07	0.25	0.43	0.45	0.75
(%)		(0.02)	(0.07)	(0.11)	(0.12)	(0.20)
Cryonival (CN)		0.11	0.09	0.11	0.12	0.11
(%)		(0.03)	(0.02)	(0.03)	(0.03)	(0.03)
Debris flow (DF)		0.25	0.57	0.40	0.60	0.85
(%)		(0.07)	(0.15)	(0.11)	(0.16)	(0.23)
Mixed (M)		0.04	0.09	0.33	0.33	0.33
(%)		(0.01)	(0.02)	(0.09)	(0.09)	(0.09)
Slope (S)		1.20	3.21	4.83	5.30	5.54
(%)		(0.32)	(0.85)	(1.29)	(1.41)	(1.48)
Glaciolacustrine (GL)		0.96	2.90	3.12	3.12	3.12
(%)		(0.25)	(0.77)	(0.83)	(0.83)	(0.83)
Glacial till (T)		13.49	29.67	51.44	57.66	62.98
(%)		(3.59)	(7.90)	(13.69)	(15.35)	(16.77)
Outcropping bedrock (B)		25.65	51.61	75.93	75.59	86.97
(%)		(6.83)	(13.74)	(20.20)	(20.13)	(23.16)
Glaciers	375.56	333.78	287.15	238.99	232.06	214.54
(%)	(100)	(88.88)	(76.46)	(63.58)	(61.69)	(57.13)

Table 7. Evolution of Quaternary sedimentary covers and outcropping bedrock during deglaciation within the 1969 glacier footprint. Numbers in brackets indicate percent area.

Documenting the structural evolution of the main drainage network during deglaciation represents an equally important step, as this affects the efficiency of postglacial sediment recruitment and transfer from the proglacial area. In the Proglacial Mazia area, we note that recession of the Mazia Glacier lobe induces hydrological disconnection and progressive deactivation of major branches of the main drainage network (**Figure 18a** and **Figure 18b**) implying that water and sediment conveyance out of the Mazia Glacier has become progressively focused on a fewer number of pathways. Moreover, as deglaciation progresses, and ice patches of dead ice are shrinking, some branches become partly buried by sediment and/or water loss to subsurface occurs (e.g., note emergence of "not visible" drainage links in **Figure 18 a** and **Figure 18d**). Collectively, over the entire study area we observe that the length of the visible drainage network increases consistently from 1996 (6.2 km^2) through 2020 (10.6 km^2) (**Table 8**). To a lesser extent, this temporal trend of drainage expansion is also observed in intermittently visible (subglacial) stream links.

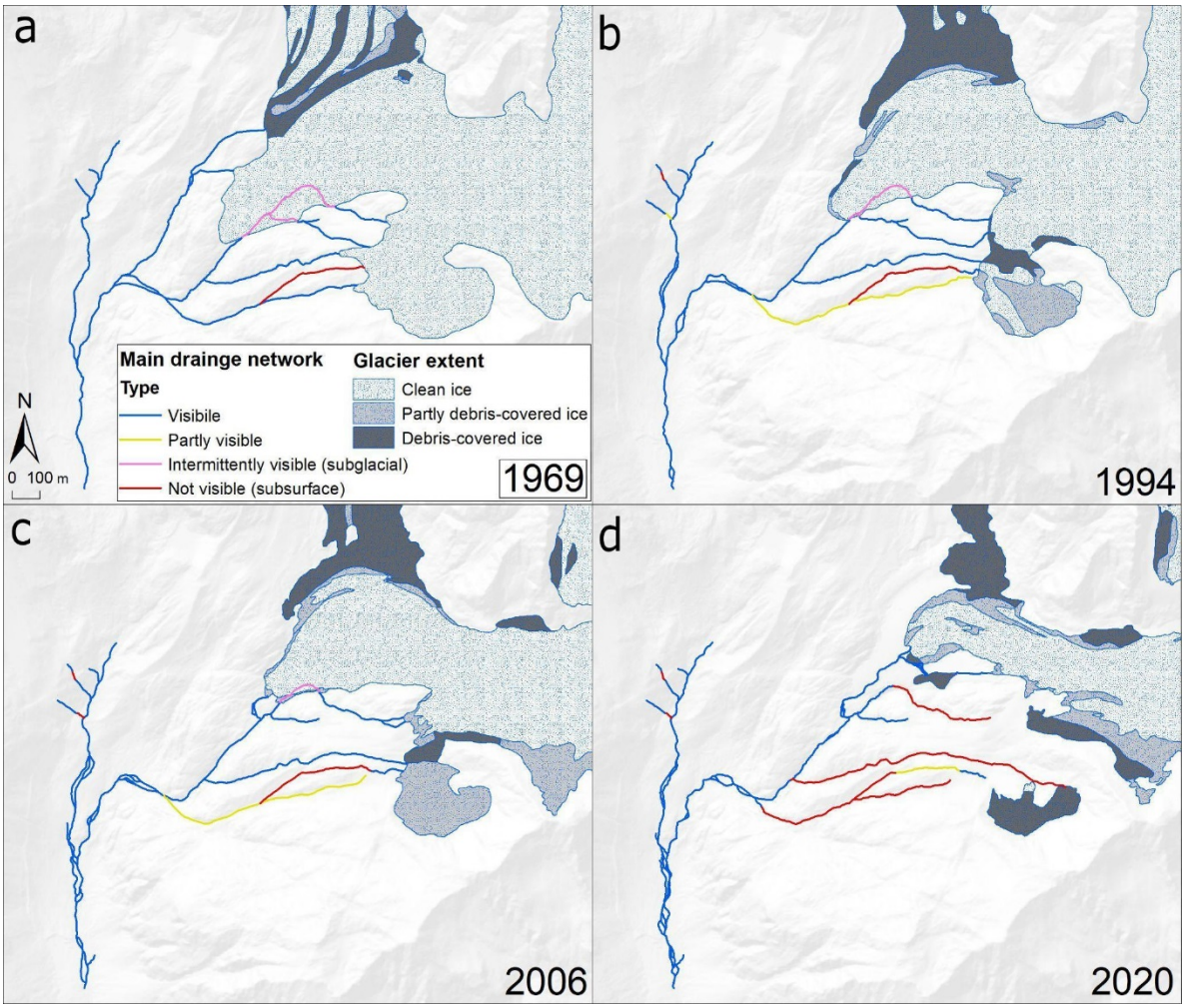

*Figure 18. Evolution of the main drainage network in relation to historical changes of the Mazia glacier tongue as mapped in photo years: (a) 1969; (b) 1994; (c) 2006; and (d) 2020. Network links are classified according to degree of visibility illustrated in **Table 3**.*

	Length (km)					
Stream flow visibility	**1969**	**1994**	**2006**	**2013**	**2017**	**2020**
Visible	6.2	5.6	7.9	10.1	9.8	10.6
(%)	(89.7)	(77.2)	(73.9)	(80.5)	(75.4)	(79.2)
Partly visible	0	1.2	0.8	0	0	0.2
(%)	(0.0)	(16.0)	(7.4)	(0.0)	(0.0)	(1.8)
Intermittently visible (subglacial)	0.7	0.5	1.0	2.3	3.1	2.4
(%)	(10.3)	(6.8)	(9.1)	(18.4)	(24.2)	(17.2)
Not visible (subsurface)	0	0	1.0	0.1	0.05	0.2
(%)	(0.0)	(0.0)	(9.5)	(1.1)	(0.4)	(1.3)
Combine	6.9	7.3	10.7	12.5	12.9	13.4

Table 8. Evolution of the main channel network between 1969 and 2020, stratified by stream flow visibility. Numbers in brackets indicate percent length of the entire channel network in a given photo year.

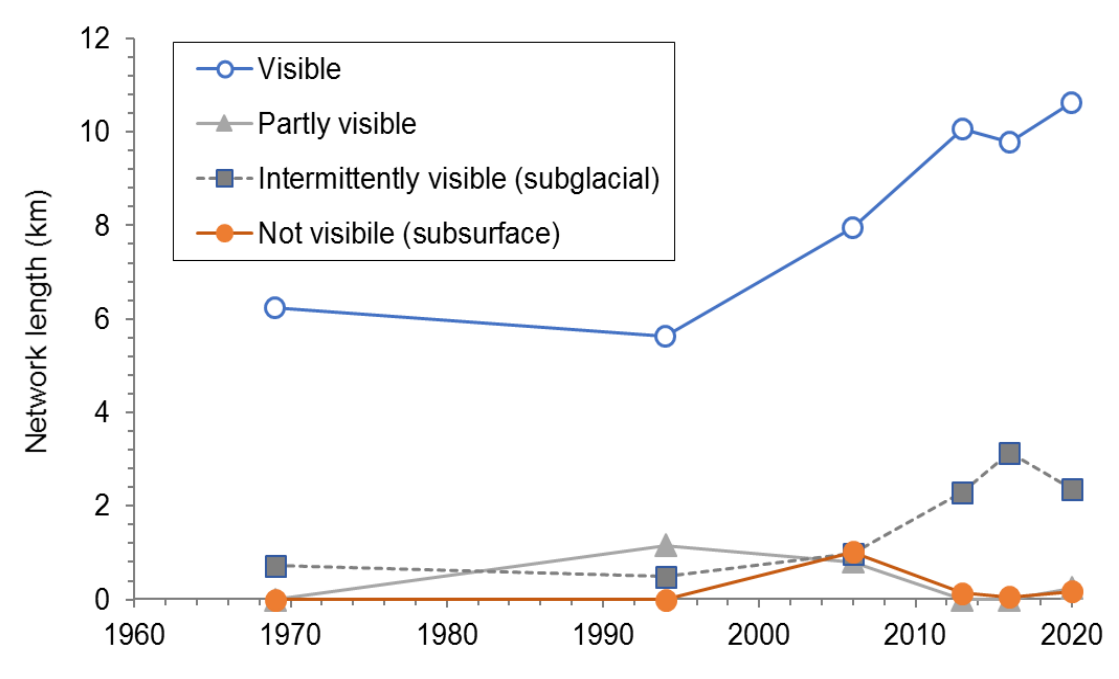

Figure 19. Evolution of the main drainage network, expressed as network length, stratified by visibility.

4.2 Sediment delivery from rapid shallow failures

The multi-temporal landslide inventory includes 193 deposition zones of shallow rapid failures. Of these, 112 were identified and mapped on the 1959 aerial photoset, and therefore, for the most part, they have occurred before 1959. By contrast, landslides identified in the subsequent aerial photo sets have a better-constrained time of occurrence, where the photo year of first identification represents the minimum age, i.e., the temporal constraint is defined by the date of the preceding aerial photo set.

Mean annual number of newly formed landslide deposits remains about constant at a value of 1.1 in the 1960-85 and 1985-99 periods, then peaks to 1.9 in the last 21 years of investigation. This increase is chiefly associated with the 19 new debris-flow deposits identified in photo year 2020, which correspond to a mean annual rate of 3.8 events occurring between 2016 and 2020.

Delivery potential	Delivery site	< 1959	1960-85	1985-99	1999-2020
Unchannel topography (LOW delivery)	Hillslope (s)	25	5	2	7
	Talus slope & cone	12	1	0	3
	Moraine (m)	11	2	3	3
Seasonal channels & transitions (MODERATE delivery)	Fan (f)	33	11	7	11
	Gully channel (gc)	3	0	0	2
	Fluvial terrace (ft)	4	0	0	0
	Floodplain (fp)	4	0	0	5
Perennial channels (HIGH delivery)	Connected tributary (ct)	9	2	1	3
	Main channel (mc)	11	6	2	5
Combined		112	27	15	39

*Table 9. Numbers of shallow rapid failures through time stratified by sediment delivery site. Temporal classification is constrained by sequential aerial photos (**Table 1**).*

Before 1959, recurring sites of landslide sediment delivery are characterized by low to moderate likelihood of reaching the perennial drainage network. Specifically, debris fans (n =33) and hillslopes (25) are by far the most common loci of landslide deposition, followed by talus slopes/cones (12), lateral moraines (11), the Saldur Creek channel bed (i.e., main channel) (11), and perennial tributaries connected directly to Saldur Creek (9) (**Table 9**). This ranking in sediment delivery does not change substantially when one examines landslides occurred after 1959. In this context, **Figure 20** is instructive in that illustrates the detail of high landslide recurrence on: (i) tributary fans located on the rocky eastern side of Upper Mazia Valley; and (ii) on the western till-mantled hillside traversed by the LIA lateral moraine (see inset in **Figure 20**).

At these sites, different delivery targets imply different depositional lengths and therefore different associated volumes of mobilized debris. Along the fan (bottom right of **Figure 20** inset), landslide tracks that stop on the fan surface are typically longer (hence larger) than those that are capable of reaching Saldur Creek. Similarly, on the opposite valley side (left portion of **Figure 20** inset), we observe that landslides that have stopped behind the moraine ridge are substantially shorter (hence smaller) than those that have either been deflected down valley, or those that have breached this glacial barrier. In this latter case, largest landslides either have reached the slope base, the main active floodplain, or have directly entered Saldur Creek.

Delivery site	Percent number		Percent volume	
	< 1959	1960-2020	< 1959	1960-2020
Hillslope (s)	22.3	17.3	5.4	9.4
Talus slope & cone (ts/tc)	10.7	4.9	9.0	2.4
Moraine (m)	9.8	9.9	5.8	6.2
Fan (f)	29.5	35.8	31.8	35.6
Gully channel (gc)	2.7	2.5	1.3	0.5
Fluvial terrace (ft)	3.6	0	6.2	0
Floodplain (fp)	3.6	6.2	4.5	12.6
Tributary channel (ct)	8.0	7.4	12.2	4.3
Main channel (mc)	9.8	16.0	23.7	29.1

Table 10. Percent number of rapid shallow failures and relevant volumes of deposited debris stratified by sediment delivery target before 1959, and between 1960 and 2020. Temporal classification is constrained by sequential aerial photos (Table 1).

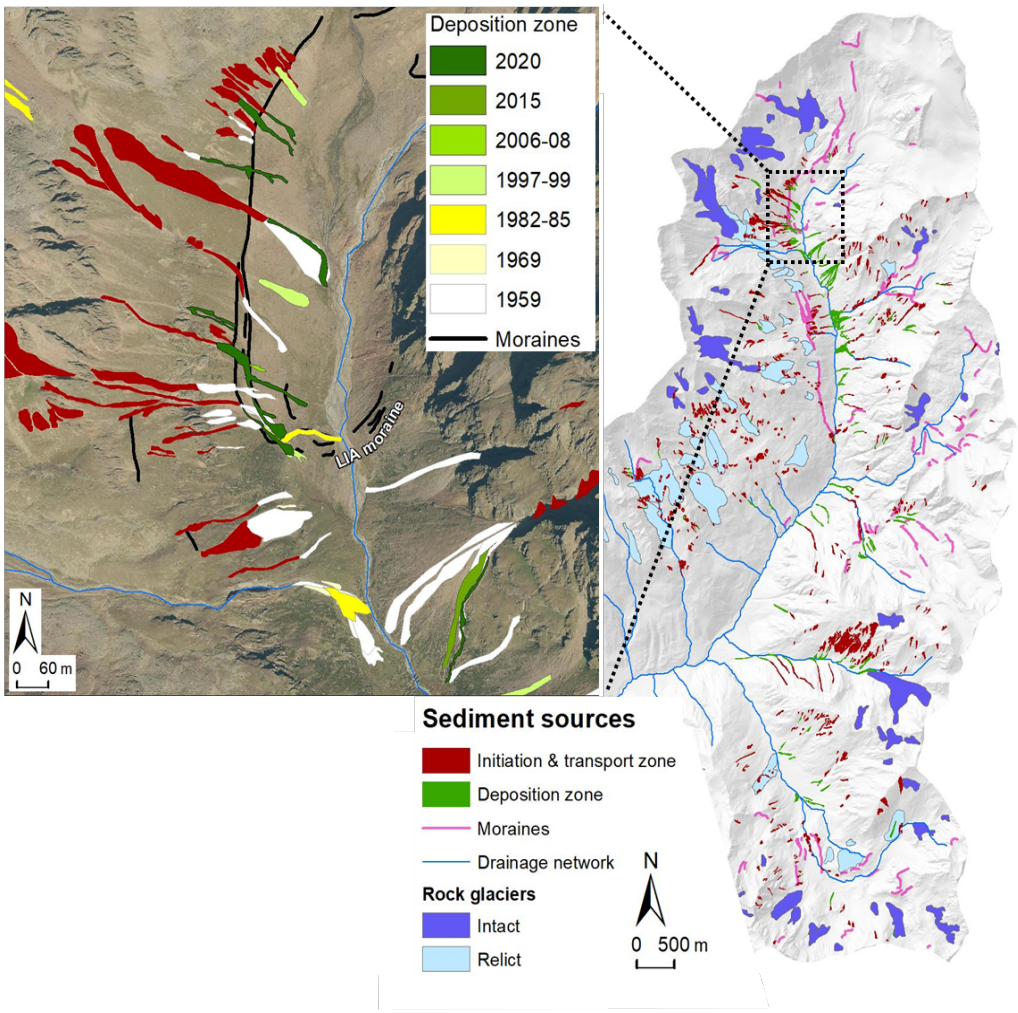

Figure 20. Inventory map of shallow rapid features (debris slides and debris flows) identified between photo years 1959 and 2020. Inset map illustrates a close-up, multi-temporal view of the deposition zones across the LIA moraine and a debris fan (bottom right corner) in Upper Mazia Valley.

The foregoing qualitative observations on a possible correspondence between sediment delivery type and landslide size is critical, as it helps explaining different percentages across sediment delivery sites observed when considering number of observations and volumes of deposited debris (**Table 10** and **Figure 21**). Following this logic, we see that landslide characterized by low delivery potential – such as hillslopes, talus slopes, and moraines – exhibit a consistent drop (i.e., down to four times) in percent volumetric weight, compared to their percent number of observations. Similarly, sites associated with high sediment delivery to streams – such as connected tributaries and main channels – see their volumetric percentages increase substantially (i.e., up to twice as much) from their percent count. In the middle lie delivery sites with moderate delivery potential – such as fans and gully channels – which display mixed changes in percent number of observations from their volumetric counterparts.

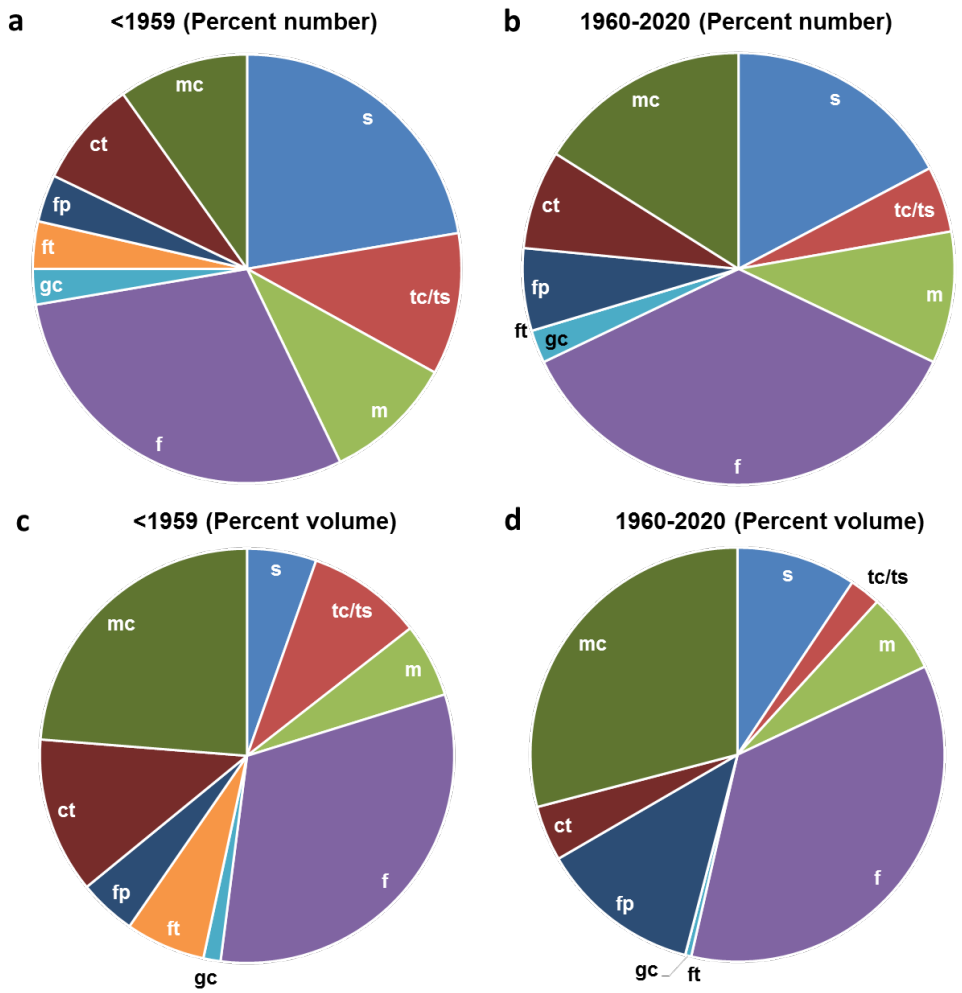

*Figure 21. Pie charts showing percentages of landslide sediment transfer across delivery sites in Mid and Upper Mazia Valley. Percentages by number and volume as mapped in 1959 (panels a and c), and in the following photo years (panels b and d). Dominant delivery sites are debris fans (f), and main perennial channels (mc). Codes refer to sediment delivery sites detailed in **Table 3.***

4.3 Los Angeles testing

LA-test values in Mazia Valley are virtually identical at sites M1 (26.2 %) and M3 (26.0), whereas an increase is observed at site M4 (29.4 %) on the Oberettes tributary fan.

4.4 Channel bed texture and armour ratio

Comparison of surficial grain size distributions (GSD) obtained respectively through field-based Wolman pebble count (Wolman, 1954) and through GrainID-based processing of close-range vertical photos (Chen et al., 2022) exhibits substantial agreement, with a tendency for the latter to generate comparably coarser distributions (**Table 11** and **Figure 22**). We observe virtually identical D50 at sites M2 and M4, and to a limited extent, coarser GrainID-based D50 at the other sites, with an offset ranging between 5 mm (M3) and 15 mm (M5). This tendency is even more apparent for coarser fractions at all sites, where offset in D84 ranges from 14 mm to 47 mm, and in D90 ranges from 26 mm to 84 mm (**Table 11**).

As for subsurface GSD, obtained from on-site sediment sieving of material coarser than 64 mm (i.e., "Lab") followed by laboratory sieving of the finer fractions (i.e., "Field"), we show the importance of integrating these two methodological steps for capturing the entire range of grain size variability. At all sites except M2 – the hanging braided alluvial plain characterized by particularly fine GSD that did not require on-site sieving – results show how laboratory sieving alone would yield markedly underestimated subsurface grain size percentiles. Underestimation ranges: (i) from as little as 15 mm up to a maximum of 38 mm, in terms of D50; (ii) from 27 to 86 mm in terms of D84; and (iii) from 28 to 105 mm in terms of D90. In turn, subsurface underestimation of sediment caliber propagates down to the calculation of armour ratios, which would result 3 to 4.3 times larger than field-integrated analogues (cf. "Lab" and "Field & Lab" values in **Table 12**).

Site	Elevation (m a.s.l.)	Slope (m/m)	Drain area (km^2)	Surface (mm)		Subsurface (mm)	
				Wolman	GrainID	Lab	Field & Lab
				D_{50}	D_{50}	D_{50}	D_{50}
M1	2730	0.10	1.3	56	62	10	42
M2	2850	0.01	0.6	21	21	7	7
M3	2405	0.11	7.6	57	62	10	42
M4	2280	0.20	1.8	57	56	9	35
M5	2240	0.08	13.8	45	60	12	50
M6	2240	0.07	1.4	na	37	7	22

Table 11. Sampling site attributes, and characteristic surface and subsurface grain size percentiles constrained by means of different techniques (see Section 3 for details).

Site	Armour ratio			
	Wolman /Lab	GrainID /Lab	Wolman/ Field & Lab	GrainID/ Field & Lab
M1	5.57	6.16	1.34	1.49
M2	3.10	3.10	3.10	3.10
M3	5.61	6.09	1.35	1.46
M4	6.12	6.01	1.64	1.62
M5	3.82	5.10	0.90	1.20
M6	na	5.01	na	1.69

Table 12. Sensitivity analysis of armour ratios to variable surface and subsurface GSD data types.

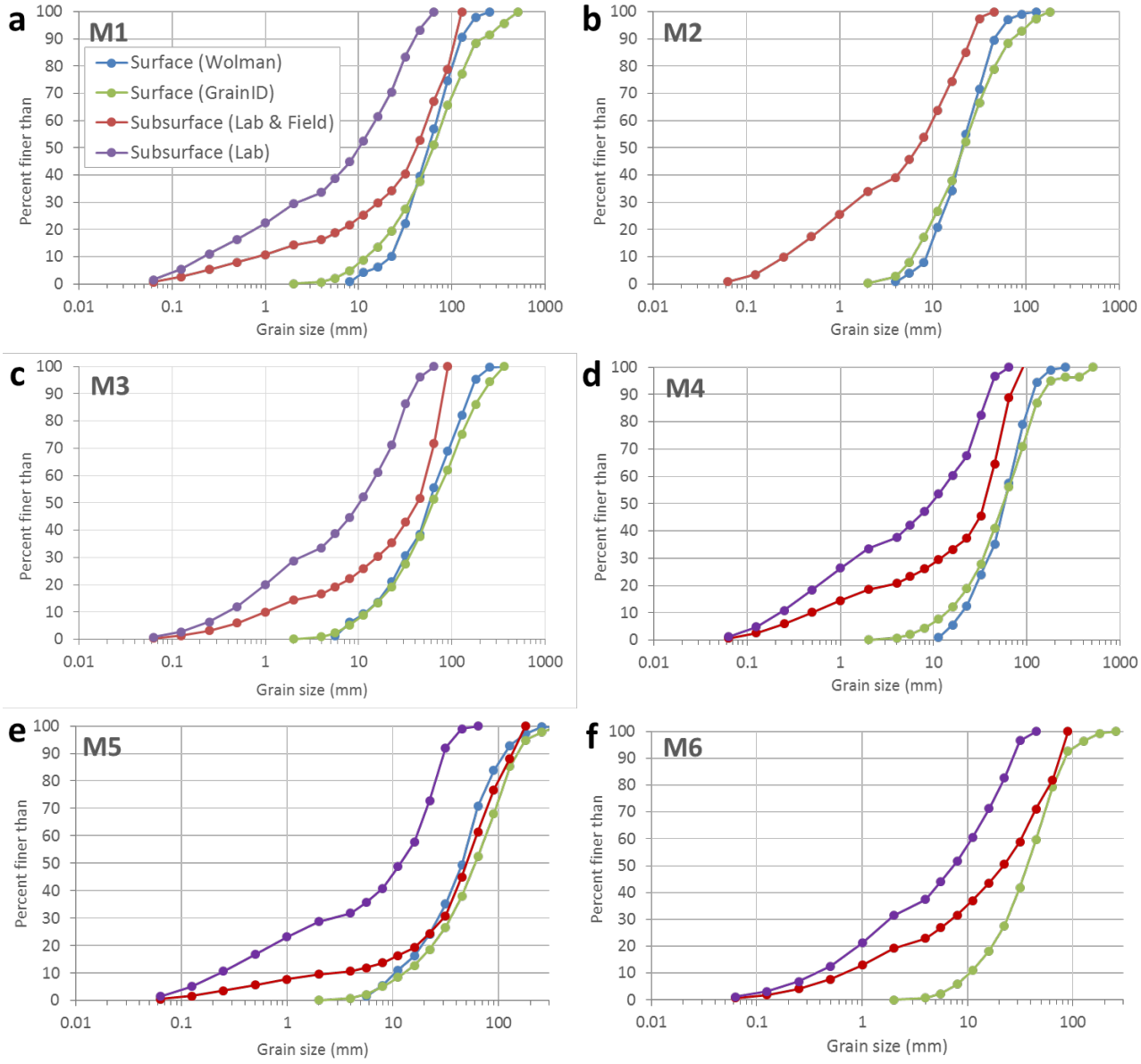

*Figure 22. Surface and subsurface grain size distributions (GSD) at the six-sampling site in Upper Mazia Valley. Corresponding percentiles and armour ratios are reported in **Tables 4.6** and **4.7**. The Wolman-based surface GSD (blue linework) derives from the collection and measurement of 250 clasts (blue linework). The GrainID-based surface GSD (green linework) derives from the analysis and amalgamation of five 1x1 m tiles distributed at representative facies locations across the lateral bar M3. The subsurface GSD derives from the preliminary on-site mechanical sieving of the coarse fraction (> 64mm) (violet linework) in conjunction with the finer counterpart (< 64 mm) sieved in the laboratory (red linework). Site M6 lacks a Wolman pebble count, owing to complete obliteration of the fan terminus that occurred at this site shortly after field photo collection in September 2021.*

Along Saldur Creek, surface D50 remains about constant from the glacier forefield (56-62 mm at M1), across the LIA moraine area (57-62 mm at M3), and down to the confluences with the two lateral tributaries (45-60 mm at M5). By contrast, D84 and D90 both show limited downstream coarsening at M3, followed by drastic fining at M5 (i.e., values at M5 are smaller than at M1; **Table 11** and **Figure 23**), hence suggesting that adjacent, steep lateral tributaries do not supply coarser bed material. This observation is supported by the GSD downstream pattern in Oberettes Creek,

where fine D50 in the braided hanging floodplain (21 mm at M2) coarsens at the fan terminus (56-57 mm) and attains values identical to those recorded at M5. The same spatial pattern applies to D84 and D90 (**Table 11** and **Figure 23**). Along these lines, we find that Unnamed Creek supplies to Saldur Creek substantially finer material, as indicated by D50 (37 mm), D84 (72 mm) and D90 (84 mm) recorded at the fan terminus (M6).

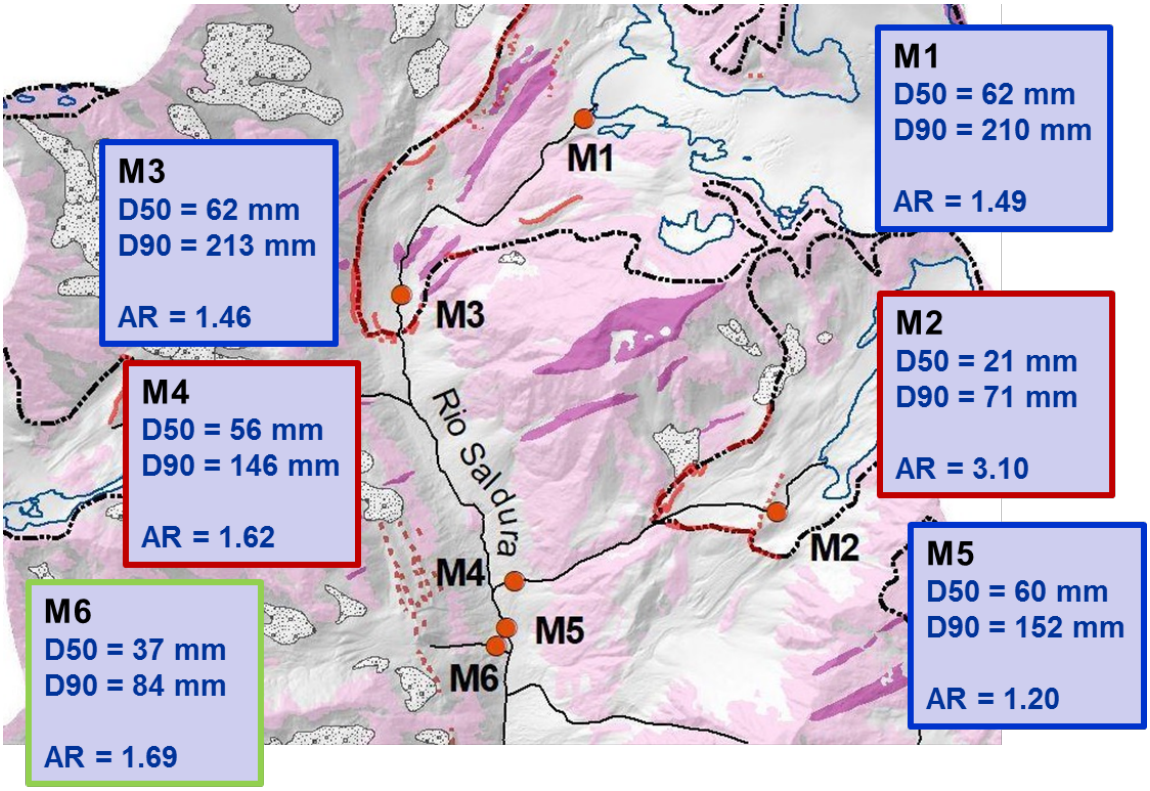

Figure 23. Map of Upper Mazia Valley showing the spatial variability of surface D50, surface D90 and armour ratio (AR) across the six sampling sites.

With reference to subsurface GSD, the spatial patterns of subsurface D50, D84 and D90 present differences and similarities with what was observed for the surface counterparts. The main difference relates to Saldur Creek main stem, where: (i) D50 remains constant between M1 and M3 (42 mm) but coarsens at M5 (50 mm); and (ii) D84 and D90 display downstream fining from M1 (98-108 mm) to M3 (72-80 mm), and substantial coarsening further downstream at M5 (113-135 mm). Similarities with surface GSD patterns relate to: (i) subsurface downstream fining between M2 and M4 along Oberettes Creek; and (ii) subsurface sediment percentiles (i.e., D50, D84 and D90) at tributary fan termini (sites M4 and M6) being substantially finer than the receiving Saldur Creek (site M5).

The combination of the foregoing surface and subsurface GSD variability generates remarkably consistent pattern of channel stability across the sampling sites, which range from gentle glacier forefields (1.3 km^2) to steep reaches nested in alluvial fans (1.8 km^2), and turbulent braided reaches along a main glacial trough (13.8 km^2). Namely, armour ratios range between 1.49 and 1.69 when using GrainID-derived data, and between 0.90 and 1.64 when using Wolman-based ones. In this context, site M2, possibly the most purely fluvial site, stands out for being the most stable with an armour ratio of 3.10 (**Table 12**).

4.5 Limitations of the software-based approach

While operating with the main photo sieving applications (see **Section 3**) the user is confronted with some specific limitations (e.g., **Figure 24**, **Figure 25** and **Figure 26**). Since all the image analysis models rely on the quality of the input image, during field photo collection, it is critical to achieve: (i) optimal light exposition, avoiding partly shaded areas; and (ii) orthogonal positioning of the camera view (use a tripod for further stability) over the target bed surface area. Experience gained during this study suggests that some typical BASEGRAIN misclassifications are attributable to: (i) fine-grained material (threshold lays below 1.6 pixels); and (ii) peculiar clast-specific color-contrast in some of the study sedimentary facies.

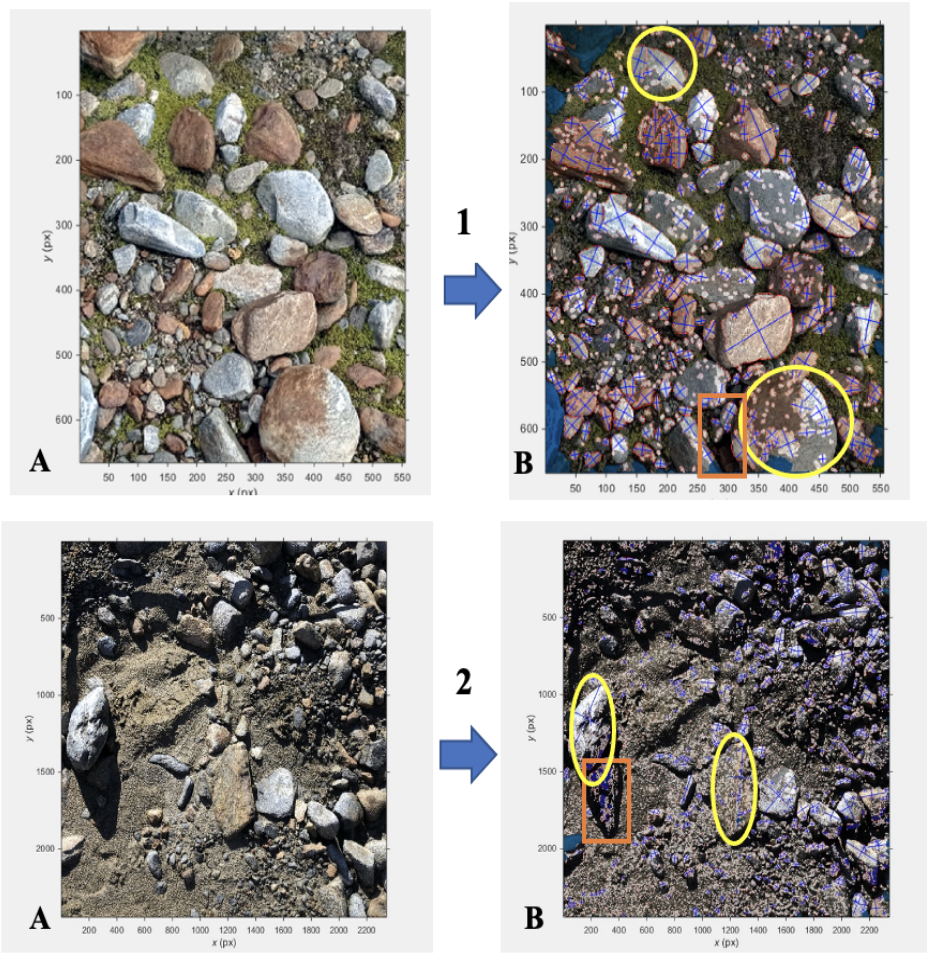

Figure 24. Examples showing typical misclassifications found through BASEGRAIN. (a) Original image; and (b) Result of automated BASEGRAIN clast recognition. Note problematic detection outputs on large grains (yellow circles) and shadow areas (orange rectangles).

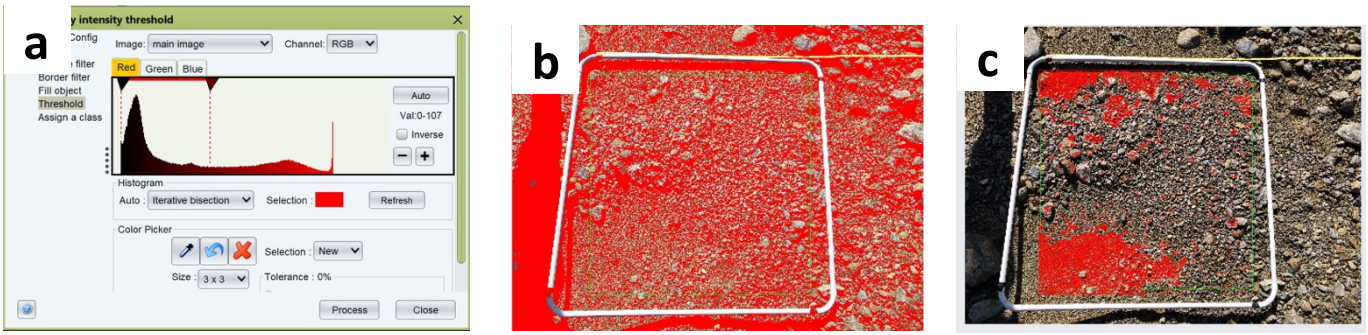

Figure 25. Example of limitations associated with the use of JMicroVision. (a) Intensity-threshold setting; (b) Matrix threshold of processed image; and (c) Final output of processed image. Note grain size misclassifications in panel c (only 25% of matrix area is detected).

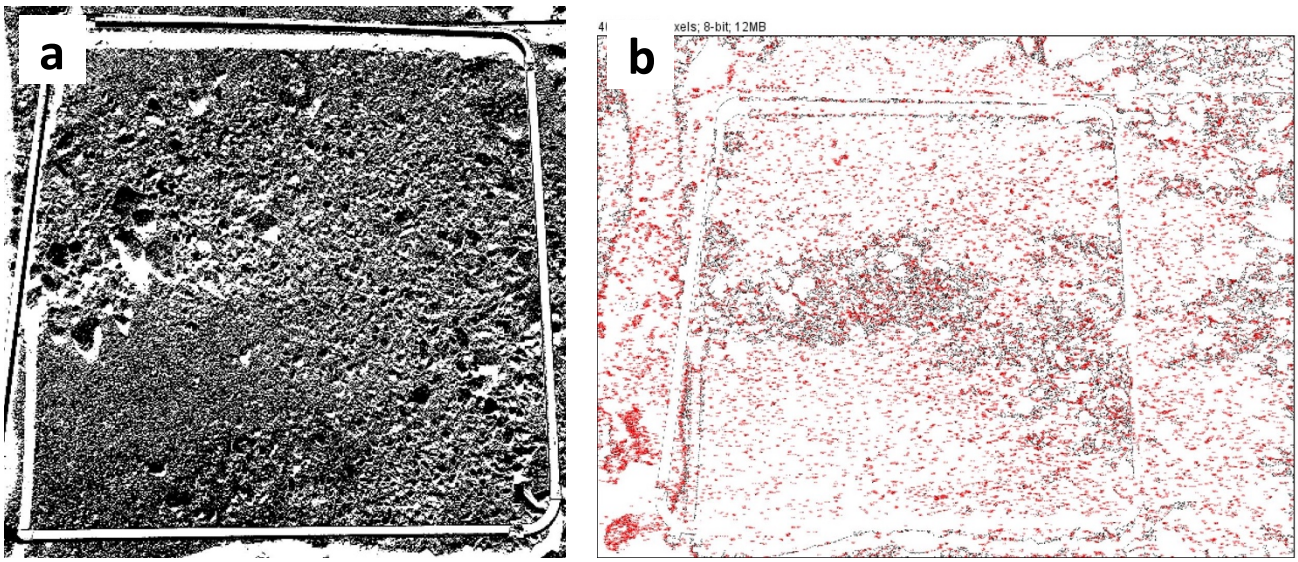

Figure 26. Example of limitations associated with the use of JMicroVision. (a) Threshold settings; and (b) processed image. Note grain size misclassifications (inaccurate detection of clast outlines).

While analyzing software-based granulometries it is essential to reckon that the clasts b-axis (intermediate axis) dimensions are the key parameter in ensuring either a passing (translation) or retainment. Users should avoid misclassifying the clasts c-axis (short axis) for the determining clast (**Figure 27**). When comparing the methods, one must consider that in both cases the b-axis is plotted during image analysis. This fact should be stated clearly to avoid misclassifications. The smaller axis on the photo corresponds to the middle axis of the clasts and not to the smallest and must therefore be compared directly with the sieve curves.

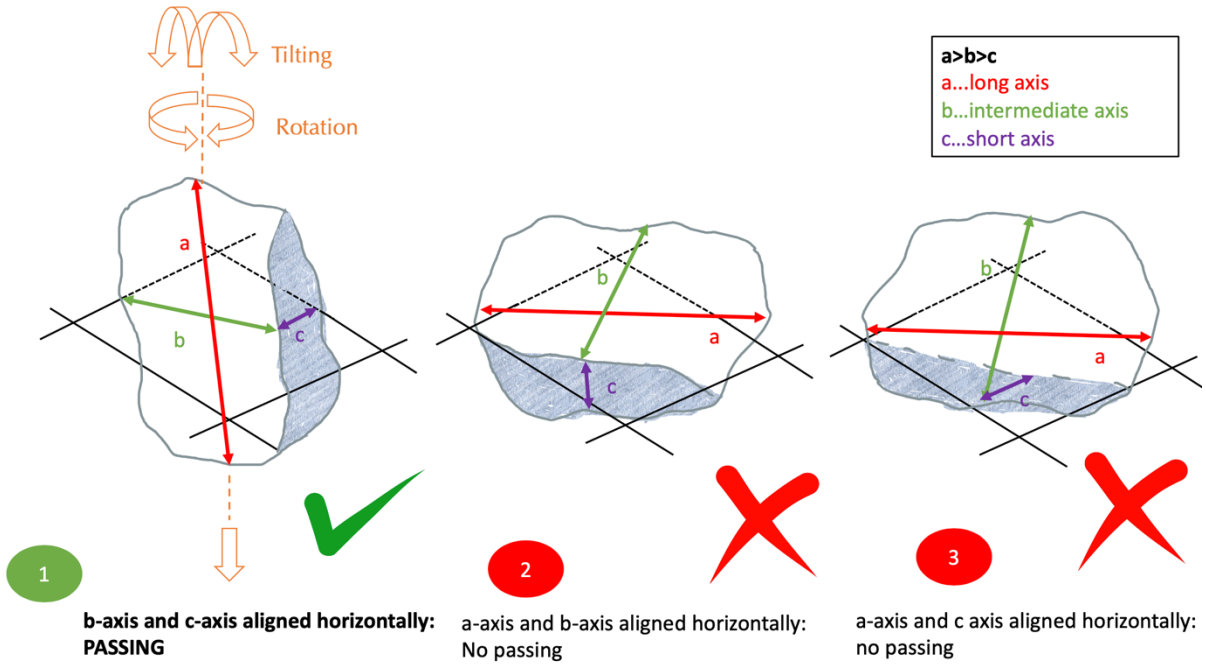

Figure 27. Conceptual scheme illustrating the geometric constraints of a clast for passing across a mesh of a give size. Note that the intermediate (b) axis constitutes the discriminant geometric attribute for a clast to pass (or be retained).

Comparison of field-based surficial GSD (cf. **Section 3.2.2**) with counterpart derived from BASEGRAIN processing (after manual clast delineation), displays respectively systematic underestimation and overestimation of the fine and coarser fractions (e.g., **Figure 28**).

Based on our experience, we suggest that the outputs of BASEGRAIN processing be evaluated with caution and recommend conducting a proper field campaign of sample collection to validate grain size distributions derived from photo sieving models.

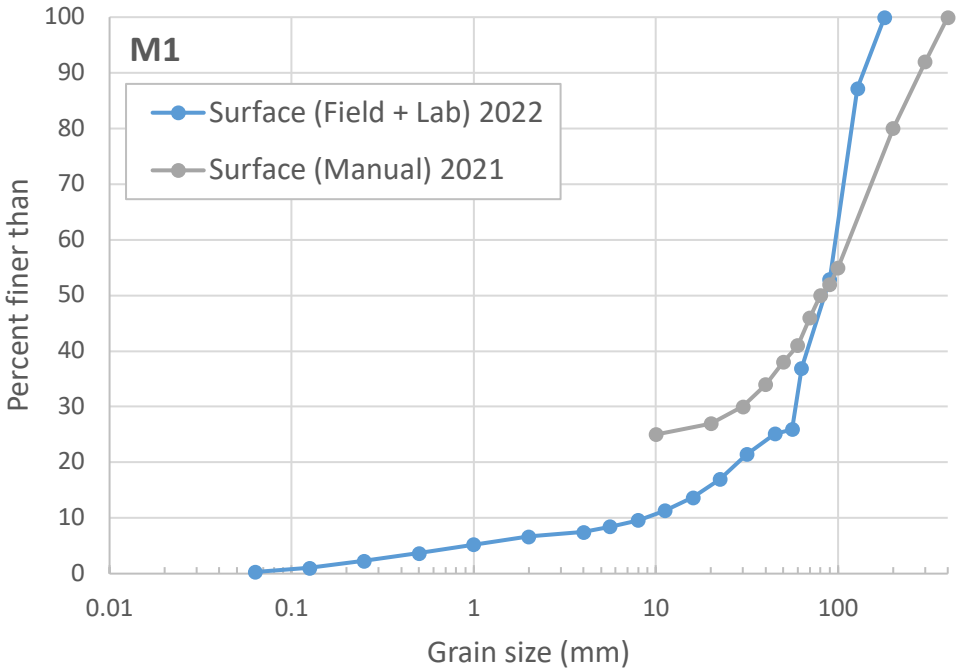

Figure 28. Surface grain-size distributions obtained through direct sampling and sieving (blue linework) and through manual clast delineation followed by BASEGRAIN processing (gray linework). Note underestimation of coarser fractions and overestimation of finer fractions around a comparable median grain-size (D50).

Acknowledgements

We acknowledge the Laboratory Team of the Office for Geology and Materials Testing – namely Ulrich Obojes, Helmuth Senoner and Valerio Tosi – for valuable field and laboratory assistance. Manel Llena provided critical field collaboration in Mazia, Lazzago and Similaun drainage basins. Federica Minotti aided with preliminary glacier mapping in Mazia Valley. Wenqi Li kindly performed the GrainID processing. Discussion with Marwan Hassan and Xingyu Chen helped improving the presentation of GSD data. Finally, special thanks go to the entire SedInOut team for the enthusiastic discussions and fruitful contributions during the whole project period.

References

Arganda-Carreras I. 2008. Unwarpj: Consistent and elastic registration in ImageJ, methods and applications. Second ImageJ User & Developer Conference.

Brardinoni F., Hassan M.A., Rollerson T. and Maynard D. 2009. Colluvial sediment dynamics in mountain drainage basins. Earth and Planetary Science Letters, 284, 310-319.

Brardinoni F., Cavalli M., Heckmann T., Liebault F., Rimbock A. 2015. Guidelines for assessing sediment dynamics in alpine basins and channel reaches. SedAlp WP4 Final Report. Alpine Space. 71 pp. www.sedalp.eu/download/dwd/reports/WP4_Report.pdf

Chen X., Hassan M.A., and Fu X. 2022. Convolutional neural networks for image-based sediment detection applied to a large terrestrial and airborne dataset. Earth Surface Dynamics, 10, 349–366. https://doi.org/10.5194/esurf-10-349-2022

Church M., McLean D., and Wolcott J.F. 1987. River bed gravels: Sampling and analysis, in: Sediment Transport in Gravel Bed Rivers, edited by: Thorne, C. R., Bathurst, J. C., and Hey, R. D., John Wiley & Sons, New Jersey, USA, 43-79, ISBN 0-471-90914-9.

Detert M. and Weitbrecht V. 2012. Automatic object detection to analyze the geometry of gravel grains – a free stand-alone tool, in: River Flow 2012, 1st Edition, edited by: Muñoz, R. M., CRC Press, London, UK, 595–600, https://doi.org/10.1201/b13250.

Detert M. and Weitbrecht V. 2013. User guide to gravelometric image analysis by BASEGRAIN, in: Advances in River Sediment Research, 1st Edition, edited by: Fukuoka, S., Nakagawa, H., Sumi, T., and Zhang, H. CRC Press, London, UK, 1789–1795, https://doi.org/10.1201/b15374.

Frank, W., Hoinkes, G., Purtscheller, F. & Thöni, M. 1987. The Austroalpine Unit west of the Hohe Tauern: The Ötztal-Stubai Complex as an example for the Eoalpine metamorphic evolution. In. Flügel & Faupl, Eds., *Geodynamics of the Eastern Alps*, Franz Deutike, Wien (1987). Pp. 179-225.

Gardent M. 2014. Inventaire et retrait des glaciers dans les alpes françaises depuis la fin du Petit Age Glaciaire. Thèse de doctorat, Géographie. Université de Grenoble. pp 445 (in French).

Gomez B. 1983. Temporal variations in bedload transport rates: the effect of progressive bed armouring. Earth Surface Processes and Landforms, 8, 41-54.

Guzzetti F, Ardizzone F, Cardinali M, Rossi M, and Valigi D, 2009. Landslide volumes and landslide mobilization rates in Umbria, central Italy. Earth and Planetary Science Letters 279, 222-229.

Haas, R. 1985. Zur Metamorphose des südlichen Ötztalkristallins unter besonderer Berücksichtigung der Matscher Einheit (Vinschgau / Südtirol): *unpublished PhD Thesis*, Universität Innsbruck, 1985.

Habler G., Thoni M., and Grasemann B. 2009. Cretaceous metamorphism in the Austroalpine Matsch Unit (Eastern Alps): the interrelation between deformation and chemical equilibration processes. Mineralogy and Petrology, 97, 149–171.

Hassan M.A. and Zimmermann A. 2012. Channel Response and Recovery to Changes in Sediment Supply. M. Church, P.M. Biron, A.G. Roy (Eds.), Gravel-Bed Rivers: Processes, Tools, Environments, 33, Wiley & Sons, Chichester, UK, pp. 464-473

Hassan M.A, Egozi R., and Parker G. 2006. Experiments on the effect of hydrograph characteristics on vertical grain sorting in gravel bed rivers. Water Resources Research, 42, p. W09408.

Hassan M.A., Saletti M., Zhang C., Ferrer-Boix C., Johnson J.P.L., Müller T., and von Flotow C. 2020. Co-evolution of coarse grain structuring and bed roughness in response to episodic sediment supply in an experimental aggrading channel. Earth Surface Processes and Landforms, 45, 948-961.

Holzhauser H., Magny M., and Zumbühl H.J.. 2005. Glacier and lake level variations in west-central Europe over the last 3500 years, The Holocene, 15, 789-801.

Hoinkes, G. and Thöni, M. (1993): Evolution of the Ötztal-Stubai, Scarl-Campo and Ulten Basement Units. In: von Raumer & Neubauer. *Pre-Mesozoic Geology in the Alps*. 485-494, Berlin, Springer

Huggel C., Carey M., Clague J.J, and Kaab A. 2015. The High-Mountain Cryosphere. Environmental changes and human risks. Cambridge University Press. 363 pp.

Hungr O. 2005. Classification and terminology. In M. Jakob, & O. Hungr. (Eds.), Debris–flow Hazard and Related Phenomena (pp. 9-24). Berlin, Heidelberg: Springer Praxis.

Hungr, O., Leroueil, S. and Picarelli, L., 2014. The Varnes classification of landslide types, an update. Landslides, 11(2), pp.167-194.

Kellerhals R. and Bray DI. 1971. Sampling procedures for coarse fluvial sediments. Journal of the Hydraulics Division, 97, 1165–1180, https://doi.org/10.1061/JYCEAJ.0003044.

Keim, L., Mair, V., and Morelli, C. 2017. General Geologic Map - Geotirol

Knoll C., Kerschner H., Heller A., and Rastner P. 2009. A GIS-based reconstruction of Little Ice Age glacier maximum extents for South Tyrol, Italy. Transactions in GIS, 13, 449-463.

Kondolf G.M., Lisle TE., and Wolman G.M. 2003. Bed sediment measurement. In GM Kondolf, and H Piegay (Eds.), Tools in fluvial geomorphology (pp. 347– 395). Chichester: John Wiley & Sons, Ltd.

Maynard, D., 1991. Tsitika river watershed: sediment source inventory. Unpublished Report for British Columbia Ministry of Forests, Research Branch, Victoria.

Neubauer, F., Hoinkes, G., Sassi, F.P., Handler, R., Höck, V., Koller, F. & Frank, W. (1999): Pre-Alpine metamorphism of the Eastern Alps. *Schweiz. Mineral. Petrogr. Mitt.*, 79, 41-62.

Nicolussi K., Le Roy M., Schlüchter C., Stoffel M., and Wacker L. 2022. The glacier advance at the onset of the Little Ice Age in the Alps: New evidence from Mont Miné and Morteratsch glaciers. The Holocene, 32, 624-638.

Ratschbacher L., Frisch W., Neubauer F., Schmid S.M., and Neugebauer J. 1989. Extension in compressional orogenic belts: the eastern Alps. Geology 17: 404–407.

Potro, M.N. (1982): Petrographie, Metamorphose, Tektonik und Metallogenese im mittleren Vinschgau / Südtirol (N – Italien). *Unveröff. Diss.*, RWTH Aachen. 304 pp.

Purtscheller, F., Haas, R., Hoinkes, G., Mogessie, A., Tessadri, R., Veltman, C. (1987): Eoalpine metamorphism in the crystalline basement. In: Flügel, H.W., Faupl, P. (Eds.), *Geodynamics of the Eastern Alps*. Deuticke Wien, Vienna, 187-189.

Roduit N. 2008. JMicroVision: Image analysis toolbox for measuring and quantifying components of high-definition images. Version 1.2.7. Software available for free download at http://www.jmicrovision.com.

Scotti R., Brardinoni F., and Crosta G.B. 2014. Post-LIA glacier changes along a latitudinal transect in the Central Italian Alps. The Cryosphere, 8, 2235-2252.

Thöni, M. 1981. Degree and evolution of the Alpine metamorphism in the Austroalpine unit W of the Hohe Tauern in the light of K/Ar and Rb/Sr age determinations on micas. *Jahrb. Geol. Bundesanst.* Wien, *124*, 111-174.

Thöni M. 1999. A review of geochronological data from the Eastern Alps. Schweizerische Mineralogische und Petrographische Mitteilungen 79: 209–230.

Wolman M.G. 1954. A method of sampling coarse river-bed material. EOS Transactions of the American Geophysical Union, 35, 951–956, https://doi.org/10.1029/TR035i006p00951.